

## Stardust Interstellar Preliminary Examination VIII: Identification of crystalline material in two interstellar candidates

Zack GAINSFORTH<sup>1\*</sup>, Frank E. BRENKER<sup>2</sup>, Alexandre S. SIMIONOVICI<sup>3</sup>, Sylvia SCHMITZ<sup>2</sup>, Manfred BURGHAMMER<sup>4</sup>, Anna L. BUTTERWORTH<sup>1</sup>, Peter CLOETENS<sup>4</sup>, Laurence LEMELLE<sup>5</sup>, Juan-Angel Sans TRESSERRAS<sup>4</sup>, Tom SCHOONJANS<sup>6</sup>, Geert SILVERSMIT<sup>6</sup>, Vicente A. SOLÉ<sup>4</sup>, Bart VEKEMANS<sup>6</sup>, Laszlo VINCZE<sup>6</sup>, Andrew J. WESTPHAL<sup>1</sup>, Carlton ALLEN<sup>7</sup>, David ANDERSON<sup>1</sup>, Asna ANSARI<sup>8</sup>, Saša BAJT<sup>9</sup>, Ron K. BASTIEN<sup>10</sup>, Nabil BASSIM<sup>11</sup>, Hans A. BECHTEL<sup>12</sup>, Janet BORG<sup>13</sup>, John BRIDGES<sup>14</sup>, Donald E. BROWNLEE<sup>15</sup>, Mark BURCHELL<sup>16</sup>, Hitesh CHANGELA<sup>17</sup>, Andrew M. DAVIS<sup>18</sup>, Ryan DOLL<sup>19</sup>, Christine FLOSS<sup>19</sup>, George FLYNN<sup>20</sup>, Patrick FOUGERAY<sup>21</sup>, David FRANK<sup>10</sup>, Eberhard GRÜN<sup>22</sup>, Philipp R. HECK<sup>8</sup>, Jon K. HILLIER<sup>31</sup>, Peter HOPPE<sup>24</sup>, Bruce HUDSON<sup>25</sup>, Joachim HUTH<sup>24</sup>, Brit HVIDE<sup>8</sup>, Anton KEARSLEY<sup>26</sup>, Ashley J. KING<sup>26</sup>, Barry LAI<sup>27</sup>, Jan LEITNER<sup>24</sup>, Hugues LEROUX<sup>28</sup>, Ariel LEONARD<sup>19</sup>, Robert LETTIERI<sup>1</sup>, William MARCHANT<sup>1</sup>, Larry R. NITTLER<sup>29</sup>, Ryan OGLIORE<sup>30</sup>, Wei Ja ONG<sup>19</sup>, Frank POSTBERG<sup>23</sup>, Mark C. PRICE<sup>16</sup>, Scott A. SANDFORD<sup>31</sup>, Ralf SRAMA<sup>32</sup>, Thomas STEPHAN<sup>18</sup>, Veerle STERKEN<sup>20,32,33</sup>, Julien STODOLNA<sup>1</sup>, Rhonda M. STROUD<sup>11</sup>, Steven SUTTON<sup>27</sup>, Mario TRIELOFF<sup>23</sup>, Peter TSOU<sup>34</sup>, Akira TSUCHIYAMA<sup>35</sup>, Tolek TYLISZCZAK<sup>12</sup>, Joshua VON KORFF<sup>1</sup>, Daniel ZEVIN<sup>1</sup>, Michael E. ZOLENSKY<sup>7</sup>, and >30,000 Stardust@home dusters<sup>36</sup>

<sup>1</sup>Space Sciences Laboratory, University of California Berkeley, Berkeley, California, USA

<sup>2</sup>Geoscience Institute, Goethe University Frankfurt, Frankfurt, Germany

<sup>3</sup>Institut des Sciences de la Terre, Observatoire des Sciences de l'Univers de Grenoble, Grenoble, France

<sup>4</sup>European Synchrotron Radiation Facility, Grenoble, France

<sup>5</sup>Ecole Normale Supérieure de Lyon, Lyon, France

<sup>6</sup>Department of Analytical Chemistry, University of Ghent, Ghent, Belgium

<sup>7</sup>ARES, NASA JSC, Houston, Texas, USA

<sup>8</sup>The Field Museum of Natural History, Chicago, Illinois, USA

<sup>9</sup>DESY, Hamburg, Germany

<sup>10</sup>ESCG, NASA JSC, Houston, Texas, USA

<sup>11</sup>Naval Research Laboratory, Washington, District of Columbia, USA

<sup>12</sup>Advanced Light Source, Lawrence Berkeley Laboratory, Berkeley, California, USA

<sup>13</sup>IAS Orsay, Orsay, France

<sup>14</sup>Space Research Centre, University of Leicester, Leicester, UK

<sup>15</sup>Department of Astronomy, University of Washington, Seattle, Washington, USA

<sup>16</sup>School of Physical Sciences, University of Kent, Canterbury, Kent, UK

<sup>17</sup>Department of Earth and Planetary Sciences, University of New Mexico, Albuquerque, New Mexico, USA

<sup>18</sup>Department of the Geophysical Sciences, University of Chicago, Chicago, Illinois, USA

<sup>19</sup>Department of Physics, Washington University, St. Louis, Missouri, USA

<sup>20</sup>SUNY Plattsburgh, Plattsburgh, New York, USA

<sup>21</sup>Chigy, Burgundy, France

<sup>22</sup>Max-Planck-Institut für Kernphysik, Heidelberg, Germany

<sup>23</sup>Institut für Geowissenschaften, University of Heidelberg, Heidelberg, Germany

<sup>24</sup>Max-Planck-Institut für Chemie, Mainz, Germany

<sup>25</sup>Midland, Ontario, Canada

<sup>26</sup>Natural History Museum, London, UK

<sup>27</sup>Advanced Photon Source, Argonne National Laboratory, Chicago, Illinois, USA

<sup>28</sup>Université des Sciences et Technologies de Lille, Lille, France

<sup>29</sup>Carnegie Institution of Washington, Washington, District of Columbia, USA

<sup>30</sup>University of Hawai'i at Manoa, Honolulu, Hawai'i, USA

<sup>31</sup>NASA Ames Research Center, Moffett Field, California, USA

<sup>32</sup>IRS, University Stuttgart, Stuttgart, Germany

<sup>33</sup>IGEP, TU Braunschweig, Braunschweig, Germany

<sup>34</sup>Jet Propulsion Laboratory, Pasadena, California, USA

<sup>35</sup>Osaka University, Osaka, Japan

<sup>36</sup>Worldwide

\*Corresponding author. E-mail: zackg@ssl.berkeley.edu

(Received 4 December 2012; revision accepted 21 May 2013)

---

**Abstract**—Using synchrotron-based X-ray diffraction measurements, we identified crystalline material in two particles of extraterrestrial origin extracted from the Stardust Interstellar Dust Collector. The first particle, I1047,1,34 (Hylabrook), consisted of a mosaiced olivine grain approximately 1  $\mu\text{m}$  in size with internal strain fields up to 0.3%. The unit cell dimensions were  $a = 4.85 \pm 0.08 \text{ \AA}$ ,  $b = 10.34 \pm 0.16 \text{ \AA}$ ,  $c = 6.08 \pm 0.13 \text{ \AA}$  ( $2\sigma$ ). The second particle, I1043,1,30 (Orion), contained an olivine grain  $\approx 2 \mu\text{m}$  in length and  $>500 \text{ nm}$  in width. It was polycrystalline with both mosaiced domains varying over  $\approx 20^\circ$  and additional unoriented domains, and contained internal strain fields  $< 1\%$ . The unit cell dimensions of the olivine were  $a = 4.76 \pm 0.05 \text{ \AA}$ ,  $b = 10.23 \pm 0.10 \text{ \AA}$ ,  $c = 5.99 \pm 0.06 \text{ \AA}$  ( $2\sigma$ ), which limited the olivine to a forsteritic composition  $> \text{Fo}_{65}$  ( $2\sigma$ ). Orion also contained abundant spinel nanocrystals of unknown composition, but unit cell dimension  $a = 8.06 \pm 0.08 \text{ \AA}$  ( $2\sigma$ ). Two additional crystalline phases were present and remained unidentified. An amorphous component appeared to be present in both these particles based on STXM and XRF results reported elsewhere.

---

## INTRODUCTION

The Stardust mission (Brownlee 2003; Tsou 2003) was a sample return mission flown as part of NASA's Discovery Mission program. It was effectively two missions in one spacecraft. The primary mission was to return the first samples from a known comet to Earth for study using instruments far too bulky to be flown in space. The primary mission resulted in an analysis of cometary material captured from comet 81P/Wild 2 with unprecedented precision and detail (Brownlee et al. 2006). The secondary mission was to return the first solid samples of material from the local interstellar medium. During  $\approx 200$  days of the 7 yr of spaceflight, the mission controllers exposed a second aerogel collector to the interstellar dust stream. The discovery and projected direction of this dust stream was based on observations by dust detectors on the Galileo and Ulysses missions (Grün et al. 1993).

Our current understanding of the interstellar medium is largely derived from astronomical observations. We expect that the dust population should comprise amorphous silicate and carbonaceous grains with an average size  $< 200 \text{ nm}$  (Kemper et al. 2004, 2005; Tielens 2005). Observations of the frequency dependence of light absorption can tell us about particle size distributions. Kim et al. (1994) found that the

particle size distribution has a sharp cut-off for grain sizes above 1  $\mu\text{m}$ , which is not to say that  $>1 \mu\text{m}$  grains are absent. With this and other information in hand, we may be tempted to form some ideas of the composition of our local interstellar medium—i.e., our immediate neighborhood containing particles that would be sampled by the Stardust interstellar collector. However, studies of dust crystallinity, grain size, and composition in the interstellar medium have focused on sight lines to the galactic center or similarly bright targets easily accessible to astronomers. Recent studies of the local interstellar medium (LISM) have shown significant chemical inhomogeneities on a parsec scale (Welsh and Lallement 2012), whereas studies of the galactic interstellar medium (ISM) have shown multiple dust populations throughout the Milky Way galaxy (Sandford et al. 1991, 1995; Pendleton et al. 1994). These cases highlight the danger in predicting the properties of the LISM dust population from the context of galactic observations. In addition, the Ulysses spacecraft has shown that dust reaching the inner system is significantly larger than the average dust size in the interstellar medium predicted by astronomical observations (Grün et al. 1993). Thus, the properties of ISM and LISM dust could vary significantly, and we should not claim a priori knowledge of what a particular grain from the LISM may look like.

Models of dust propagation in the heliosphere show that interstellar particles have been size sorted by radiation pressure and Lorentz interactions within the heliosphere. Most small particles should not penetrate to 2 AU where the Stardust collection occurred, and this probably introduced a bias favoring collection of the largest local interstellar medium (LISM) particles (Sterken et al. 2014). Particles could also have been significantly slowed, even to as low as  $\approx 2 \text{ km s}^{-1}$ . Even at these speeds, there is still potential for particle modification by aerogel capture, which would complicate their study (Frank et al. 2013; Postberg et al. 2014). The collector itself introduces another bias. If a typical  $<200 \text{ nm}$  interstellar particle were to strike the aerogel collector of the Stardust spacecraft, it may or may not create an impact feature that could be recognized and extracted for analysis (Westphal et al. 2014a). Therefore, the Stardust Interstellar collection has a very strong bias toward the largest particles in the LISM, and even these may have suffered some impact modification.

We focus on two particles identified as having a possible interstellar origin based on their trajectories as measured in aerogel, modeling of interstellar dust propagation in the solar system, and inconsistency in composition with spacecraft materials (Burchell et al. 2013; Frank et al. 2013; Sterken et al. 2014, Westphal et al. 2014a). While it is not yet certain whether these are interstellar or interplanetary particles, the evidence currently points toward an interstellar origin (Westphal et al. 2014a).

## EXPERIMENTAL METHODS

We performed this work as part of the Interstellar Preliminary Examination (ISPE) (Westphal et al. 2014b). Because the ISPE analyses were limited to nondestructive techniques, we analyzed the interstellar dust candidates using synchrotron X-ray and infrared microprobes.

The particles are I1047,1,34 (named “Hylabrook”) and I1043,1,30 (“Orion”), and were captured in aerogel by impact with the Stardust collector at approximately 2 AU (Tsou 2003). After recovery and identification (Westphal et al. 2014b), they were extracted from the Stardust Interstellar Dust Collector in small triangular wedges  $\approx 1 \text{ mm}$  in size called picokeystones (Westphal et al. 2004; Frank et al. 2013). The extraction and sample preparation of these and other particles are described in detail in companion papers in this same volume (Frank et al. 2013; Westphal et al. 2014). We compared optical images of the track shapes to laboratory calibrations and concluded that the capture velocities of both Hylabrook and Orion were  $<10 \text{ km s}^{-1}$  (Postberg et al. 2014). This is approximately the same

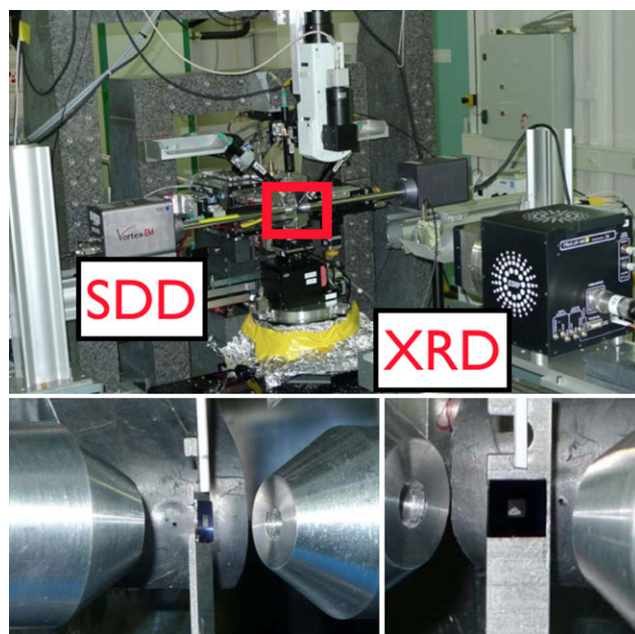


Fig. 1. Top image shows the experimental setup of ID13 at the ESRF. One of two silicon drift detectors (SDDs) used to acquire XRF spectra is labeled on the left; the X-ray diffraction camera (XRD) is labeled on the right. The sample is within the area denoted by the red box. The lower left image shows a close-up of the sample mounting with the X-ray beam exiting through the pinhole and striking the sample. Two XRF detectors are oriented on either side of the sample,  $90^\circ$  from the beam. The image on the lower right shows the sample from a normal incidence angle so the orientation of the keystone is visible.

capture velocity as experienced by the Stardust cometary collection.

## XRD Data Collection

We studied the two interstellar dust candidates by X-ray diffraction (XRD) and X-ray fluorescence (XRF) on two synchrotron beamlines (ID13 and ID22) at the European Synchrotron Radiation Facility (ESRF). ESRF beamline ID13 (Fig. 1) is designed for X-ray nanodiffraction with beamspots on the order of 400 nm diameter. It utilizes an undulator source and can produce photons from 5 to 17 keV. The photons are monochromated with a liquid  $\text{N}_2$  cooled Si-111 double monochromator providing an energy resolution of  $dE/E \approx 10^{-4}$ . We acquired simultaneous XRF and XRD data of Hylabrook (track I1047,1,34) at a series of angular rotations to obtain a pattern analogous to a traditional powder pattern. We acquired XRF and XRD maps of Orion (track I1043,1,30) by rastering the sample perpendicular to the X-ray beam with a 200 nm pixel step size and a  $400 \times 450 \text{ nm}$  beam waist. We recorded the XRD image at each pixel using a FreLon

4M camera developed at the ESRF, with  $2048 \times 2048$  pixels/frame, a  $50 \times 50 \mu\text{m}$  pixel size, and a 16 bit readout. The convergence angle of the beam was  $\approx 1 \times 1$  mrad. XRD patterns were acquired in transmission geometry. We calibrated the beamline using  $\text{Al}_2\text{O}_3$  and polycrystalline Al metal diffraction standards. We recorded XRF spectra simultaneously using two Vortex-EM  $50 \text{ mm}^2$  silicon drift detectors (SDDs).

ESRF beamline ID22 (NanoImaging endstation) is designed for X-ray nanodiffraction and XRF imaging and produces photons in the energy range of 4–37 keV (Bleuet et al. 2008). We acquired an XRF and XRD map of Orion by rastering with a  $150 \text{ nm}$  pixel size and using a beam spot of  $225 \times 235 \text{ nm}$ .  $2048 \times 2048$  pixel images were acquired. We calibrated the beamline using a polysilicon standard. Orion was mapped using two different beamlines as part of an agenda to characterize sample alteration and to resolve outstanding science questions arising from previous analyses.

Keystones were mounted similarly in ID13 and ID22. On ID22, the X-ray beam was exactly normal to the silicon nitride membrane. On ID13, the X-ray beam was at a  $45^\circ$  angle. The XRD detector was then placed directly behind the sample. Fig. 1 shows the experimental arrangement on ID13.

XRF analyses are discussed in companion articles by Brenker et al. (2014) and Simionovici et al. (2014). Scanning transmission X-ray microscopy (STXM) studies of these samples are discussed in Butterworth et al. (2014).

To identify phases from the XRD data, we employed two complementary approaches: A comparison of d-spacings against a library of known minerals, and ab initio derivation of unit cell parameters.

### Phase Identification from Virtual Powder Patterns

We processed the raw data into virtual powder patterns (see Figs. 3 and 7) via two algorithms to achieve differing objectives. In the first, we made an average image by averaging all the XRD patterns: if  $D_i$  was one pattern in a rotational dataset (Hylabrook) or translational dataset (Orion), then  $D_i(x, y)$  was the intensity of a given pixel  $(x, y)$  in that pattern. The corresponding pixel in the average image  $A(x, y)$  was

$$A(x, y) = \frac{1}{N} \sum_{i=1}^N D_i(x, y) \quad (1)$$

where  $i$  cycled through the  $N = 160$  acquired patterns at  $0.5^\circ$  rotational increments for Hylabrook or  $N = 324$  patterns for each sample translation for Orion. The average image was the best approximation of an actual

powder pattern, and the observed peak characteristics (position, FWHM, shape) were faithful to an actual powder pattern.

To improve signal to noise for weak reflections, we also employed a second algorithm that suppressed noise. The standard deviation (SD) image was defined as:

$$S(x, y) = \sqrt{\frac{1}{N} \sum_{i=1}^N (D_i(x, y) - A(x, y))^2} \quad (2)$$

so that each pixel was the standard deviation of the same pixel in the component images rather than the average. In this case, pixels that were intense in only one or several images were greatly amplified relative to noise fluctuations. The centroids of the peaks were preserved as the standard deviation was a monotonic function of the variation in intensity. However, the shape and width of the peaks and the intensity of one peak relative to another were not preserved.

The average and SD images were then azimuthally integrated to produce a 1D powder pattern that could be used for fitting minerals (see figs. 4 and 8). As our sample was a small particle embedded in aerogel, there was a strong background signal from amorphous  $\text{SiO}_2$  diffraction, Rayleigh and Compton scattering. This background was not analyzed but simply removed by means of a spline fit using the software package Fityk (Wojdyr 2010). Similarly, we did not attempt to analyze any amorphous diffraction. As we did not sample all crystalline orientations as a true powder pattern would have, we limited ourselves to peak positions and peak shapes during subsequent analysis and did not attempt to analyze peak intensities.

Powder diffraction patterns can be fit using a fingerprinting approach: observed d-spacings are compared against a database of minerals. We first compared the experimental data against 80 fingerprints including presolar grain minerals that have been seen in meteorites, interplanetary dust particles, astronomical observations, or are theoretically expected as summarized in the review article by Lodders and Amari (2005), and the references therein. We also included materials used in sample preparation and several additional common meteoritic minerals. For each mineral, we simulated a powder diffraction pattern using the energy and instrumental broadening coefficients derived from our beamline using the software packages CrystalDiffract (CrystalMaker Software Ltd. 2012) and/or PDF-4+/Minerals (International Center For Diffraction Data 2012). We read the 80 fingerprints into MATLAB® (The MathWorks, Inc. 2011), and applied a peak finding algorithm (Yoder 2011) to isolate a set of model peaks.

We then matched the experimentally measured d-spacings with the nearest model d-spacing, and if none could be found within 2% of the measured d-spacing, we considered that reflection unmatched.

We used a figure of merit defined by Smith and Snyder (1979), a standard metric in the powder diffraction field, to quantitatively assess the goodness of fit defined as  $F_N = (1/|\Delta 2\theta|)(N/N_{\text{poss}})$ , where  $N$  is the number of peaks found experimentally and  $N_{\text{poss}}$  is the number of possible peaks we may expect to see in the pattern theoretically.  $|\Delta 2\theta|$  is the mean difference between the matched peak positions and their ideal values.  $F_N$  thus has units of inverse degrees, and the inverse of  $F_N$  is the average discrepancy between measured peak positions and model peak positions in degrees. Based on the fact that our instrumental FWHM was  $0.07^\circ$  at  $20^\circ$ , we constrained a positive match to values of  $F_N > 14$ . Each fingerprint test produced a set of three numbers: (1)  $F_N$ , (2) the number of model peaks not seen in the measured data, (3) the number of measured peaks not seen in the model data. If a measured peak was not predicted by the fingerprint, then the fit was rejected, irrespective of the other parameters. The converse was not true: absence of a model peak in the measured data was expected as we had sparse powder patterns and may have missed weaker reflections. However, such absences were still penalized in the  $F_N$ . Finally, the effect of camera length uncertainty was removed by adjusting d-spacings for the measured data by  $\pm 3\%$  in steps of  $0.01\%$ , and then choosing the best match.

The fingerprints were forsterite (two fingerprints from separate sources), fayalite, tephroite, kirschsteinite, monticellite, laihunite 1M, laihunite 3M, liebenbergite, chrysotile, talc, glaucocroite, ringwoodite, wadsleyite, SiC 3C, diamond, diopside, albite, anorthite, clinoenstatite, orthoenstatite, pigeonite, gehlenite, graphite, corundum, spinel (two from separate sources), spinel rocksalt, ülvospinel, defective spinel, chromite, magnetite, hercynite, trevorite, silicon, greigite, alpha-quartz, kamacite, taenite, tetrataenite, schreibersite, troilite, hibonite, grossite, sodalite, orthoclase, perovskite, TiC, TiN, AlN, niningerite, fersilicite, oldhamite, halite, daubrelite, alabandite, sylvite, chlorite, biotite, augite, awaruite, calcite, cohenite, alpha-cristobalite, grossular, hematite, maghemite, magnesioferrite, wüstite, periclase, neirite, ferrosilite, hedenbergite, suessite, pyrope, pyrite, pentlandite, hexagonal pyrrhotite, monoclinic pyrrhotite 4C, monoclinic pyrrhotite 6C.

### Ab Initio Unit Cell Determination

In a second approach, we analyzed the unit cell from the diffraction data without assuming that the pattern was one of our 80 chosen fingerprints. Instead, we

included and excluded the various crystal systems based on the observed d-spacings. This approach allowed us to uniquely identify the unit cell to very high certainty. First, we explored which of the seven crystal systems could produce the observed pattern under any circumstances with the assumption that only a single phase was diffracting. Next, we chose the highest possible symmetry unit cell with the smallest volume as the most likely candidate for this crystal (Le Bail 2004). We ordered the symmetry of the seven crystal systems from highest symmetry to lowest symmetry: cubic, hexagonal/trigonal, tetragonal, orthorhombic, monoclinic, triclinic. We explored which of these crystal systems would produce our experimental pattern using the software package McMaille (Le Bail 2004). The two lowest symmetry systems (triclinic and monoclinic) were computationally prohibitive, and so it was impossible to fully explore the space. However, we did apply McMaille's Monte Carlo approach, which was very fast and has been proven to have a high success rate (Le Bail 2004).

We then placed error bars on the unit cell parameters using a Monte Carlo code we wrote in MATLAB<sup>®</sup> (The MathWorks, Inc. 2011). This code determined what effect the camera length calibration, and random errors in peak position determination had on our determination of the unit cell. Beginning with the set of experimentally measured d-spacings, our Monte Carlo simulation added systematic (camera length) and stochastic (detector geometry) errors to produce 50,000 trial diffraction patterns. For each pattern, it computed optimal unit cells using an unconstrained nonlinear optimization implemented as the function `fminsearch` in MATLAB<sup>®</sup> (Lagarias et al. 1998). The unit cell angles  $\alpha$ ,  $\beta$ , and  $\gamma$  were fixed at  $90^\circ$  in accordance with either a cubic or orthorhombic structure (we did this computation only for spinel and olivine). For the systematic camera length error, the same random offset up to  $\pm 1\%$  was added to all d-spacings. For the nonsystematic errors, a random offset up to  $\pm 1\%$  (Hylabrook) was computed for each d-spacing separately. Orion had a better calibration and the random offset was  $0.2\%$ . This produced histograms allowing for the determination of error bars on the various lattice parameters.  $2\sigma$  bounds were computed by integrating the histograms.

### Size-Strain Analysis

One can measure the average strain within crystals by comparing the breadth of the reflections (FWHM) to the breadth of reflections produced by a perfect crystal (Williamson and Hall 1953; Scherrer 1918; Stokes and Wilson 1944; Balzar 1999). In practice, it is necessary to remove the competing broadening caused by small crystallite sizes, and the instrumental optics. Broadening

due to small crystallite volumes influences the breadth of all peaks equally, whereas broadening due to strain influences those reflections with small d-spacings more dramatically. Thus, one can plot the broadening as a function of  $2\theta$ , and nanocrystallite volume will be read as inversely proportional to the y-intercept, while the slope will be related to the strain. This simplest approach is the Williamson-Hall method. Other approaches use similar logic, but apply more robust mathematical models to describe the broadening of the peaks.

For quantitative analysis, we used the double-Voigt method of strain analysis (Balzar 1999) because it is more robust to noisy datasets and also utilizes the distinction between two types of microstrain: local and nonlocal. Strain fields due to domain boundary stresses, for example, permeate the entire crystal and commonly generate a broadening profile best described by a Lorentzian peak shape. Strain fields due to point defects, which only strain a localized region of a few nanometers, produce a more Gaussian shaped peak (Adler and Houska 1979; Balzar 1999).

The double-Voigt method utilizes pseudo-Voigt functions, which are a combination of Gaussian and Lorentzian curves and are the basis for separating the two forms of microstrain. Analysis results in a volume-weighted domain size,  $D_v$ , representing the particle diameter (analogous to a  $D$  in the Scherrer equation) and a surface-weighted domain size,  $D_s$ , also representing the particle diameter. For a monodisperse spherical population, the actual domain diameter is related to the volume- and area-weighted sizes by  $D = (4/3)D_v = (3/2)D_s$  while for lognormal distributions  $D < D_s < D_v$  (Balzar 1999). In principle, one could use the relative values of  $D_v$  and  $D_s$  to infer particle shapes or size distributions.

The instrumental factors must be deconvolved from the experimentally measured broadening to obtain the sample's inherent broadening and therefore measure the size and strain contributions to that broadening. We used a corundum standard ( $\alpha\text{-Al}_2\text{O}_3$ ) as our calibration for instrumental broadening, but also carried out the calculations without deconvolution of the instrumental broadening. The latter gave a firm lower limit on the domain size, and an upper limit on the strain fields present, as the additional instrument broadening would only make the particles appear smaller and more strained than they really were. As the corundum almost certainly exhibits some size broadening (Thompson et al. 1987), our results after subtracting the instrumental broadening may have overestimated the particle size and underestimated the strain.

Ring patterns for the corundum standard were analyzed with the Area Diffraction Machine software (Webb 2007) to produce  $I(2\theta)$  plots where  $I$  is the

intensity and  $2\theta$  is the angle of the diffraction from the incident beam. The peak positions and shapes were determined by fitting a pseudo-Voigt plus linear background with the Fityk software package (Wojdyr 2010). The instrumental broadening measured from corundum was then removed from the Hylabrook peak breadths using the relations from Thompson et al. (1987) and fed into the BREADTH software package (Balzar 1999), which implemented the double-Voigt method to analyze size and strain.

The full width at half maximum (FWHM) of the pseudo-Voigt representing the instrumental broadening was found to be  $0.07^\circ$  at  $2\theta \approx 20^\circ$ . While dedicated powder synchrotron lines may be expected to achieve a FWHM of approximately  $0.01^\circ$ , ID13 was a nanofocus beamline so the incident beam was not perfectly parallel, which caused additional instrumental broadening. In addition, some portion of this FWHM may have been due to the small domain size of the corundum standard.

### Processing Topographical Datasets

In the case of Orion, we produced X-ray diffraction topographs (Black and Long 2004) using software we wrote in MATLAB<sup>®</sup>. An X-ray diffraction topograph is similar to a darkfield image in transmission electron microscopy. One produces an image from X-rays diffracted into a specific direction. To accomplish this, we generated a "SD" image as described above and selected circular regions around notable reflections. Each region acted as a mask against all images in the dataset. For each image, we summed the pixels within the mask into a scalar value that represented the intensity of that reflection. Then we mapped each scalar value to the spatial position of the sample. In this way, we built up an  $18 \times 18$  pixel image (324 pixels) from the 324 diffraction patterns, where the intensity of a pixel represented the intensity of the X-ray reflection at a spatial coordinate. As the pixels were 200 nm wide, the topographs were  $3.6 \mu\text{m}$  wide. There was a point spread function (PSF) convolved with the topographical images as the beam waist was larger than the pixel size. Thus, there was significant flux in the tails extending out at least one pixel on either side of the central pixel. We measured the PSF using the best reflection available—i.e., one in which the reflection is nearly perfectly circular showing no evidence of asterism (smearing). The corresponding topograph generated from this reflection is shown in Fig. 2. The point source image appeared as a single bright pixel with dimmer neighbors. Some intensity was evident two pixels away, but was very much reduced. Because of the beam waist and the resulting point spread function, we could not resolve crystallite sizes below 400 nm, or two pixels.

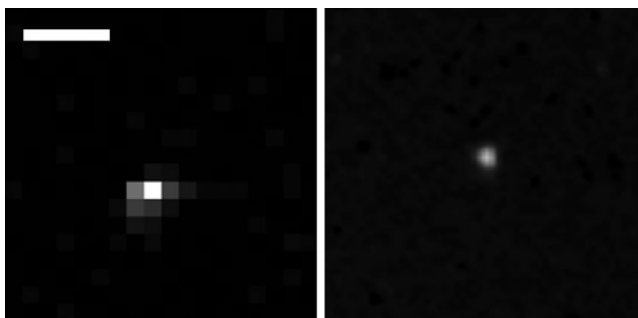


Fig. 2. The point spread function (PSF) of the topographs was estimated from the most pointlike topograph (left) using an olivine 020 reflection at 5.12 Å. On the right, the corresponding diffraction spot shows no evidence of asterism and is nearly perfectly circular. The point spread is slightly greater than one pixel wide; significant flare occurs in neighboring pixels and minor flare can occur two pixels away. The scalebar is one micron.

Table 1. Simulated intensities for the 011 reflection of kamacite nanograins in our experimental setup.

Size (nm)	$I_{\max}$ (%)	FWHM (°)
1000	100	0.07
50	64	0.11
20	31	0.23
10	16	0.43
5	8	0.84
2	3	2.12

### Nanocrystalline and Amorphous Phases

We also investigated whether our XRD pattern may have missed very small nanoparticulates. Table 1 shows simulated intensities for the 011 reflection of kamacite for our beam conditions and shows that particles more than about 10 nm in size should have remained easily visible in our diffraction pattern. Even small grains such as 2 nm nanodiamonds should have been visible if their modal abundance were high.

### RESULTS: TRACK 34 (HYLABROOK)

Track I1047,1,34 contains one terminal particle named Hylabrook. We first studied it by STXM, and then by XRF/XRD on ESRF beamline ID13. We acquired a set of diffraction patterns using a tomographic mount with photons at 13,895 eV ( $\lambda = 0.89229$  Å). We rotated the sample through 80° in 0.5° increments, and acquired a diffraction pattern and XRF spectrum at each rotation. The pattern was sufficiently complete to determine unit cell parameters and obtain a likely mineral fit. Figure 3 shows the SD image for Hylabrook. The SD image was used when we wished to know the d-spacings and azimuthal angles of reflections. The average image

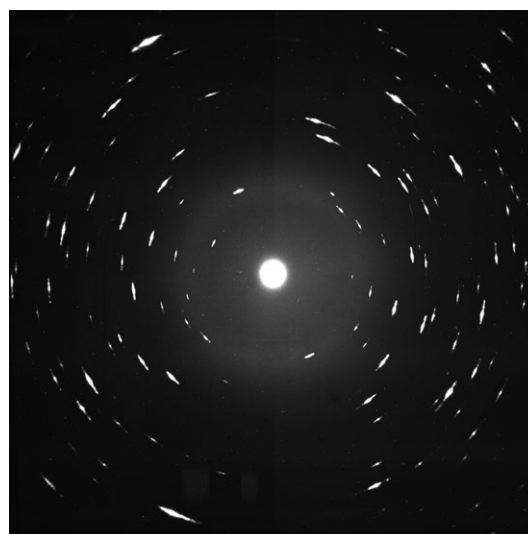


Fig. 3. SD image for Hylabrook generated by taking the standard deviation of 160 images acquired at 0.5° rotational intervals between 0 and 80°. In contrast to typical powder patterns, we did not see fully populated rings. Nevertheless, the pattern was sufficiently well filled out to permit analysis of the phase(s) present.

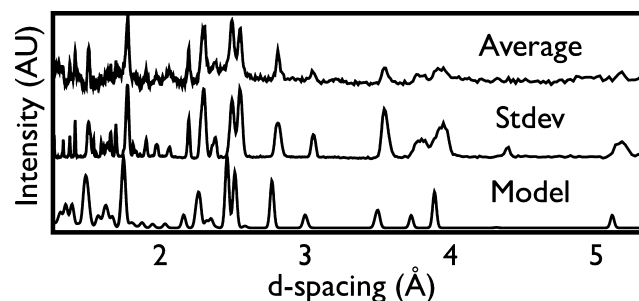


Fig. 4. 1D powder integration patterns for Hylabrook derived from the average image, the SD image, and an ideal model pattern for  $\text{Fo}_{100}$ . The peak at 4.3 Å in the SD pattern is a low intensity reflection, which is present in the forsterite model, but with intensity too low to be visible in this plot. A slight systematic shift of the SD and average images to the right is due to an intentionally uncorrected camera length calibration uncertainty.

was used when we wished to know the FWHM and shape of peaks. Figure 4 shows three 1D powder integration patterns produced from the average image, the SD image, and a model pattern for pure forsterite.

### Fit Against Likely Minerals

Column 1 of Table 2 shows the d-spacings observed in our SD pattern. We fit these against our 80 fingerprints (Table 3). We found that only the olivine group minerals fit all the measured peaks well.  $\text{Fo}_{100}$  produced a good match with  $F_{14} = 41$ , and all measured peaks were fit by the model. This meant that

Table 2. Measured and model peak positions for phases in Hylabrook.

$d_{\text{meas}}^a$	$d_{\text{model}}^b$	hkl
5.18	5.11	020
4.39	4.32	110
3.94	3.89	021
3.80	3.73	101
3.55	3.50	111
	3.48	120
3.06	3.01	121
	3.00	002
2.81	2.77	130
n.d.	2.59	022
n.d.	2.56	040
2.55	2.52	131
2.50	2.46	112
2.38	2.38	200
2.36	2.35	041
	2.32	210
2.30	2.27	122
	2.25	140
2.20	2.16	211
	2.16	220
n.d.	2.11	141
2.06	2.03	132
	2.03	221

<sup>a</sup>Centroids of the experimentally measured peaks for Hylabrook.

<sup>b</sup>Centroids of the expected reflections based on a  $F_{0100}$  composition.

Where the experimental pattern was unable to resolve close reflections, two model peaks are assigned.

we fit 14 peaks to obtain a figure of merit of 41, well above our acceptance threshold. No other phase met the threshold requirements for a fit.

### Ab Initio Unit Cell

We used observed d-spacings to determine the unit cell directly by testing all possible unit cells. We explored the cubic system (0.005 Å steps, over the range of 2–20 Å), the hexagonal/trigonal systems (0.01 Å steps, over the range of 2–18 Å), the tetragonal system (0.05 Å steps, over the range of 2–16 Å), and the orthorhombic system (0.05 Å steps, over the range of 2–20 Å). The orthorhombic system resulted in an excellent fit for a unit cell with dimensions  $a = 4.84$ ,  $b = 10.33$ ,  $c = 6.06$ . This unit cell produced a high  $F_N$  with a small unit cell volume, and was consistent with the olivine mineral family. Other candidates could be discarded on the basis of a significantly worse  $F_N$ , large unit cell volume, and/or a lack of minerals to match them. While we did explore the monoclinic and triclinic systems using Monte Carlo, we did not find any fits better than the above orthorhombic fit. The resultant error distributions were only slightly asymmetric (Fig. 5), so we assumed symmetry and quoted the error

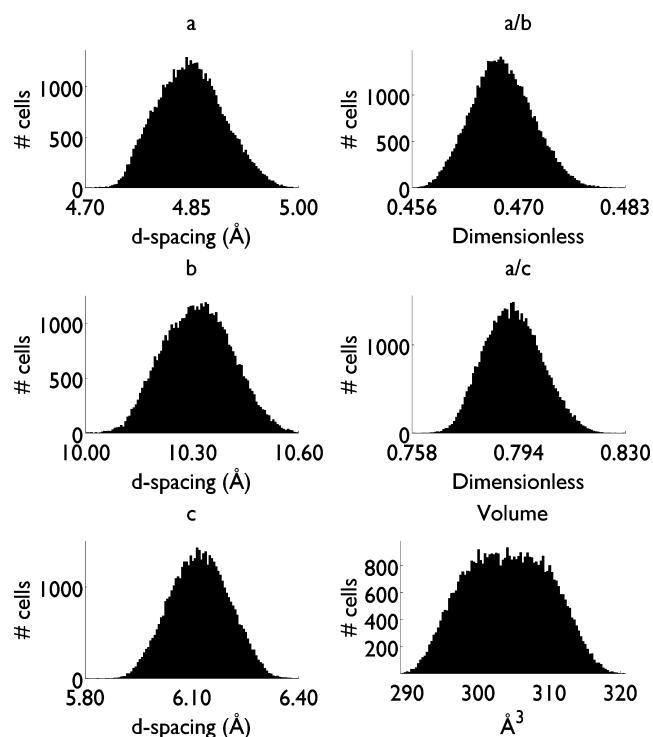


Fig. 5. Error distributions for the unit cell parameters in Hylabrook derived from a 50,000 trial Monte Carlo. The best fit values do not exactly match the centroids of the distributions since they are asymmetric.

bars as  $\pm 2\sigma$  values given in Table 4:  $a = 4.85 \pm 0.08$  Å,  $b = 10.34 \pm 0.16$  Å,  $c = 6.08 \pm 0.13$  Å ( $2\sigma$ ).

The PDF-4+/Minerals database (International Center For Diffraction Data 2012) tracks a large set of known minerals along with their properties. The only mineral matches in this database with unit cell dimensions within 0.1 Å of the experimentally determined values were olivine group minerals, with the space group Pbnm. Three reflections 022, 040, and 141, were not observed in the experimental pattern, but were generally low intensity peaks and if the sample were not perfectly oriented to show them, we would expect them to be absent. Thus, with the exception of these weak 022, 040, and 141 reflections, there was an exact one-to-one correspondence between the observed pattern and a model pattern for olivine, so we concluded that Hylabrook probably had an olivine structure.

### Defective Structure in Hylabrook

Hylabrook's diffraction pattern (Fig. 3) showed the presence of asterism of the reflections on the order of 1 to 10° in azimuth. Figure 6 is a magnified view of several peaks and shows a clockwise pattern of a single narrow intense peak followed by a broader peak and then a tail. Such structures come about when there are multiple

Table 3. Closest fingerprint matches for Hylabrook XRD. The minerals are listed with the best fit at the top and the worst at the bottom. The primary parameter for determining fit quality is how many measured peaks are not predicted by the model spectrum. Only those minerals where every peak is predicted by the model are included in this table.  $F_N$  acted as a second parameter which determined goodness of fit as explained in the text. The only minerals to fit all the experimental peaks are members of the olivine group and anorthite, and of those, the best fit by a large margin is forsterite.

Database	ID	Mineral	Formula	Crystal system	Space group	$F_N$
PDF-4+	04-007-9021	Forsterite	$Mg_2SiO_4$	Orthorhombic	Pbnm1	41
AMCSD	0000171	Forsterite	$Mg_2SiO_4$	Orthorhombic	Pbnm	34
PDF-4+	04-009-8350	Fayalite	$Fe_2SiO_4$	Orthorhombic	Pbnm	19
PDF-4+	04-007-9023	Tephroite	$Mn_2SiO_4$	Orthorhombic	Pbnm	15
PDF-4+	04-011-2883	Anorthite	$CaAl_2Si_2O_3$	Triclinic	$P\bar{1}$	6

Table 4. Dimensions for the unit cell of the crystal in Hylabrook with error bars.

Parameter	Value	$\pm 2\sigma$ abs	$\pm 2\sigma$ rel
a	4.85	0.08	1.7%
b	10.34	0.16	1.5%
c	6.08	0.13	2.1%
a/b	0.469	0.008	1.7%
a/c	0.797	0.021	2.6%
V	304.97	10.7	3.5%

crystalline domains with a net orientation—unlike a polycrystalline material in which the domains do not have net orientation (Cullity and Stock 1978).

Because Hylabrook was examined on a goniometer under microfocus conditions, slight drift of the sample position caused small variations in the camera length throughout the scan. These did not affect the overall calibration as the order of these variations was smaller than the uncertainty of the camera length calibration. However, they did increase the FWHM when the peaks occurred in multiple frames because the centroid of the peak varied slightly from frame to frame. Therefore, the breadth of the Hylabrook reflections was not determined from the average image, but from distinct frames comprising it. Nine such peaks were examined and chosen to represent the most diverse set of peaks in Hylabrook. Some were polygonalized/mosaiced and showed varying degrees of broadening. Table 5 shows the reflections measured along with the FWHM representing the broadening of that peak.

The reflection at  $2\theta = [22.39, 22.50]$  was asymmetric and gave a poor fit with a single pseudo-Voigt, but was well fit with two pseudo-Voigts. The centroids were  $0.1^\circ$  apart and could have been due to a fortuitous overlap of the 200 and 112 reflections. From Table 5, it was evident that the reflection contained one bright well-focused component and one dimmer component with a greater asterism. The lack of any asymmetry in the corundum standard proved that the asymmetry was native to Hylabrook and not an instrumental effect.

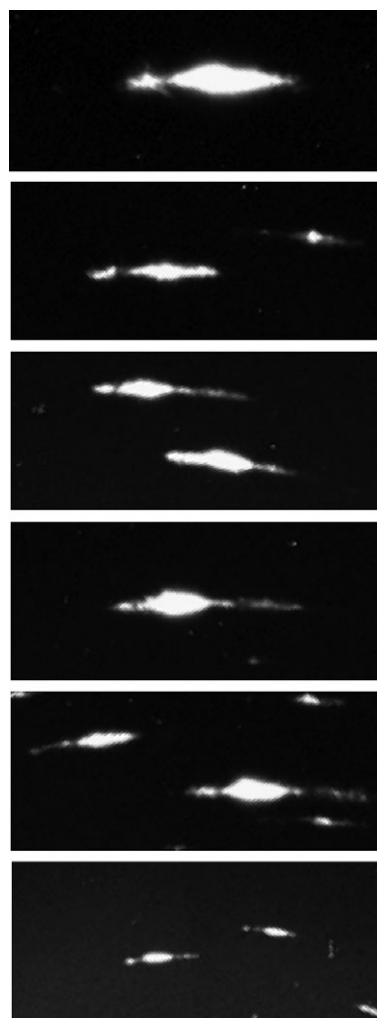
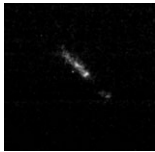
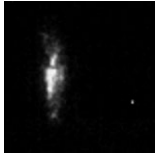


Fig. 6. A number of reflections in Hylabrook had the same polygonalization. In the image above, they have been rotated about the pattern center so they can be compared. The relative sizes of each are faithful to the original image (Fig. 3). Moving clockwise, the polygonalization manifested as a single small peak, followed by a larger broader peak, and then usually a tail.

Table 5. Reflections measured for size-strain analysis of Hylabrook.

$2\theta^a$	FWHM	Reflection	$2\theta$	FWHM	Reflection
13.24	0.119		29.38	0.179	
13.56	0.087		33.66	0.155	
20.62	0.123		33.98	N/A	
22.39	0.122		34.48	0.155	
22.50	0.115				
23.46	0.180		36.63	N/A	

<sup>a</sup> $2\theta$  positions and FWHM for the pseudo-Voigt used to fit the broadening.

Therefore, it was not likely to be a single domain reflection. For this reason, we felt justified in fitting the peak using two pseudo-Voigt functions with a single linear background, and including both peaks in the size-strain analysis.

The reflections at  $2\theta = 33.98$  and  $36.63$  also gave poor fits to a pseudo-Voigt and while the cause could have been due to an overlap of neighboring reflections, there was no indication of this in the corresponding 2D image shown in Table 5. Instead, the unexpected line shape could have been due to noise present in the experimental data, or another sample-dependent variation. For this reason, we chose to exclude these reflections from the size-strain analysis.

The double-Voigt analysis resulted in a volume-weighted domain size of  $D_v = 710 \pm 420 \text{ \AA}$  ( $2\sigma$ ) and a surface-weighted domain size of  $D_s = 350 \pm 210 \text{ \AA}$  ( $2\sigma$ ). Based on our instrumental calibration, we could not accurately discern crystallite sizes above about 80 nm (volume-weighted) as the crystallite broadening becomes comparable to the instrumental broadening. Therefore, the  $2\sigma$  upper limit on volume-weighted

crystallite size ( $D_v$ ) was essentially compatible with a large grain size—i.e., no resolved size broadening.

The strain measured by the double-Voigt analysis was  $0.2\% \pm 0.08\%$  ( $2\sigma$ ). We are not aware of a quantitative interpretation of this magnitude of strain in olivine. For elastic deformation, Abramson et al. (1997) found that bulk strains in olivine on the order of 0.2% were representative of stresses  $\leq 1$  GPa, depending on the axis of the stress. However, our olivine was clearly not under external pressure such as from a diamond anvil cell, so the strain we saw was a residual field left over from plastic deformation.

As noted above, corundum can cause broadening of its own. If we leave the instrumental broadening convolved with the original peaks, we obtain a very conservative lower limit on particle size and an upper limit on strain. Doing so, we found that domain sizes were  $\geq 27 \text{ nm}$  ( $2\sigma$ ) and internal strain averages  $\leq 0.3\%$  ( $2\sigma$ ).

In conclusion, we did not clearly resolve any size broadening in Hylabrook, but saw moderate strain from crystalline defects. Furthermore, polygonalization indicated subgrain boundaries as opposed to randomly

oriented separate crystallites. With a 0.3% upper limit on the strain, Hylabrook had a high crystal quality, although we expect that a number of defects were present and could have been imaged, for example, with a transmission electron microscope.

### Capture Effects

Hypervelocity capture of particles in aerogel can result in changes to the particle structure. Primarily, the outer layers are ablated away to produce smaller, more rounded grains. However, the shock and thermal stresses of the capture event can also modify internal microstructure. Here, we discuss whether our polygonalization or microstrain measurements were capture effects, or if they were native characteristics of the extraterrestrial particle. Because the capture velocity of Hylabrook was  $<10 \text{ km s}^{-1}$ , we can apply the work of Stodolna et al. (2012) who studied the microstructural modifications of olivine shot into aerogel and showed that it is possible to form rims of mixed olivine fingers with interwoven  $\text{SiO}_2$  glass up to about 150 nm thick when captured into aerogel at about  $6 \text{ km s}^{-1}$ . As this is not much less than the radius of Hylabrook, we may worry that the polygonalization and strain fields we saw were simply due to capture. However, Stodolna et al. (2012) also found that the mixed olivine +  $\text{SiO}_2$  maintained the same diffraction pattern as the host grain with no rotation of the zone axis and significantly less peak broadening than we saw. In most cases, the mixture zone did not appear at all, but rather a sharp transition between intact olivine and compressed aerogel was evident (see fig. 5 of Stodolna et al. 2012). It is unlikely, therefore, that the polygonalization we saw in Hylabrook was induced by aerogel capture and so we conclude that it was native to the particle before capture. The same study also found occasional dislocations induced in the olivine crystals from the capture. In the worst case, they found a strain of approximately 1% within the dislocation loop, and computed that the pressure necessary to induce these defects was approximately 1.5 GPa. They postulated that the strains were generated by transient stresses from the extreme thermal gradient that can arise during capture rather than impact shock itself. Models based on momentum balance (Anderson 1998) and compression of a highly porous medium (Trigo-Rodriguez et al. 2008) both suggest that peak shock pressures at impact speeds of  $6 \text{ km s}^{-1}$  are of order 800 MPa and only rise above 1.5–2 GPa for impact speeds in excess of 8–10  $\text{km s}^{-1}$ . On the other hand, we measured an average strain value which is sensitive to the regions devoid of defects as well as the regions with

defects. Therefore we are uncertain whether the strain we see is due to aerogel capture or is primary.

### EXCESS IRON CONTENT

XRF data showed that Hylabrook was  $\approx 25\%$  Fe by weight (Brenker et al. 2014). STXM analysis following the ID13 analysis revealed that the Fe had mobilized and did not correlate spatially with Mg (Butterworth et al. 2014). To verify that this modification did not alter our diffraction results, we examined a sequence of diffraction patterns acquired throughout the rotational scan and did not find any evidence for modification of the crystalline phase. Thus, the modification either occurred after the ID13 XRD acquisition, or did not alter the olivine phase. While we did not see any other phases in diffraction, it is possible that the Fe resided in an amorphous phase, or Fe-bearing nanoparticles.

### Summary of Hylabrook

We conclude that Hylabrook is an olivine crystal several hundred nanometers across, with at least several subgrains, and an internal strain field of  $\approx 0.2\%$ .

### RESULTS: TRACK 30, ORION

I1043,1,30, Orion, was first analyzed on XRF/XRD beamline ID13 at ESRF at 13,895 eV ( $\lambda = 0.89229 \text{ \AA}$ ), with a bandwidth of  $\approx 1 \text{ eV}$ . We rastered the sample through the beam to produce an  $18 \times 18$  pixel map with  $200 \times 200 \text{ nm}$  pixels. This oversampled the beam waist, which was  $400 \times 450 \text{ nm}$ . At each pixel of the map, we acquired a 2D diffraction pattern. Therefore, we had the ability to spatially separate different crystallite domains by comparing them with neighboring images, and for those grains  $>400 \text{ nm}$  in size we could directly measure their size using X-ray topography (Black and Long 2004) as described below. The track was then analyzed by STXM (Butterworth et al. 2014): elemental maps were acquired as well as XANES. The track was then sent back to ESRF for XRF/XRD on ID22 and imaged with a 350 eV bandwidth at 17000 eV ( $\lambda = 0.72932 \text{ \AA}$ ) to produce XRF and XRD maps with a  $150 \times 150 \text{ nm}$  pixel and 180 nm beam waist. We acquired diffraction patterns at each pixel and computed topographs from selected reflections.

At some time after the end of the ID13 acquisition but before the STXM acquisition, the particle was modified and separated into two objects: some crystalline material was amorphized and displaced several microns. The cause of this disruption remains unidentified, but is discussed more thoroughly in

Brenker et al. (2014), Butterworth et al. (2014), and Simionovici et al. (2014). This provided us with an easy method to separate phases, as we saw in total four diffracting phases in the first ID13 scan, and fewer in the ID22 scan. Therefore, it was easier to definitively map specific peaks to specific phases. As the first three scans on ID13 showed essentially identical diffraction and XRF maps, we concluded that no modification to the particle occurred during this time. Therefore, the initial scans from ID13 were valid, and we used the first and only the first ID13 scan to analyze d-spacings and FWHMs quantitatively. The second and third ID13 scans were discarded, although still useable, and the ID22 data were used only for determining which peaks map to the surviving phase.

### Phase Determination from Topographs

The SD images of Orion taken on ID13 and ID22 are shown in Fig. 7. We saw significant broadening and polygonalization, indicating multiple distinct diffractive domains as well as the presence of strain. The 1D powder integration patterns are shown in Fig. 8. The peak positions are given in Table 6 and confirm the presence of olivine and eight additional peaks. Therefore, Orion was likely a multiphase object. We compared the ID13 data with the ID22 data and found that all the olivine peaks present in the ID13 scan were absent in the ID22 scan with the possible exception of one. We interpreted this to mean that the olivine was amorphized at some point after the initial ID13 XRD maps. Additional evidence from STXM corroborated this (Butterworth et al. 2014). Meanwhile, all eight peaks from the ID13 data that did not map to olivine remained in the ID22 data. Of those eight, only five were visible in the radial integration pattern, and of those five only four were strong enough to easily analyze.

Using the McMaille software package (Le Bail 2004), we could not find a unit cell for the eight nonolivine peaks, but fitting only the four intense reflections at 4.663 Å, 2.841 Å, 2.434 Å, and 2.015 Å resulted in a cubic unit cell with  $a = 8.06$  Å. Searching the PDF/4+ Minerals database for cubic minerals near  $a = 8.06$  Å shows spinel minerals are closest. Many chemical compositions are compatible with this unit cell, including magnesiospinel, chromite, hercynite, gahnite, and ringwoodite. We could not constrain the chemistry with our data.

We produced topographs from 30 olivine reflections at d-spacings of 5.12 Å, 3.72 Å, and 3.50 Å corresponding to hkl's 020, 101, and 111/120, respectively. These d-spacings were well separated from spinel reflections and could be used to discriminate

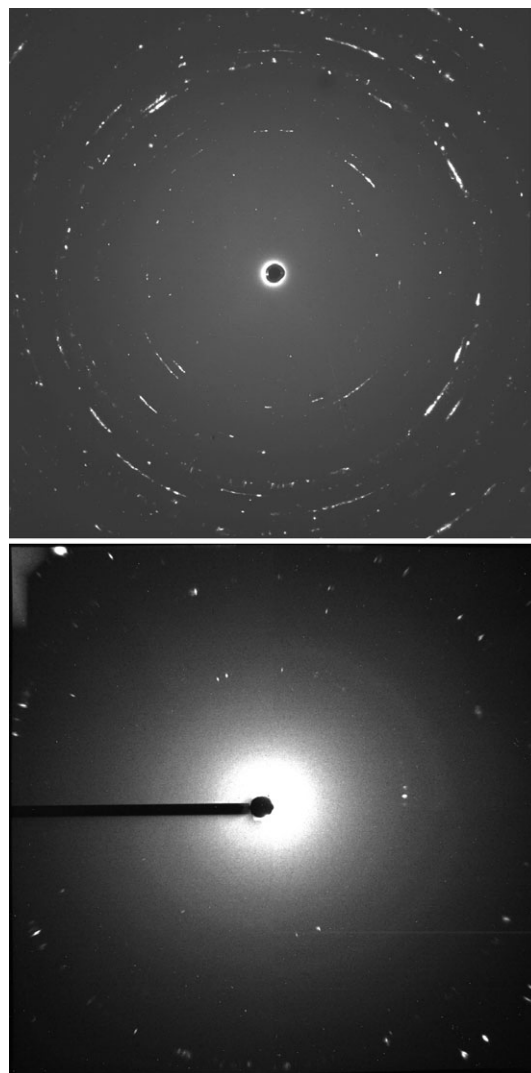


Fig. 7. Top image is the SD image of Orion from ID13. Bottom image is the SD image from ID22.

between the two phases (Fig. 9A). Likewise, we produced a topograph from the longest two d-spacings from spinel: 4.67 Å (111) and 2.84 Å (022), which were unambiguously separated from olivine (Fig. 9B).

The remaining weak peaks at 8.844, 3.229, 2.215, and 3.167 Å could not be explained as spinel or olivine. Using topographs, we discovered that they were spatially separated from the olivine and spinel and therefore were a third phase. We attempted to find a mineral match using PDF 4+ and to determine a unit cell using the McMaille software package, but did not find any satisfactory results. Therefore, it may be multiphase, or have a very large, low symmetry unit cell. We call this phase the unknown core phase as it is situated near the olivine in the core of the particle (Fig. 9C).

XRF and STXM found the bulk composition of Orion was  $\approx 25\%$  Fe by weight (Brenker et al. 2014;

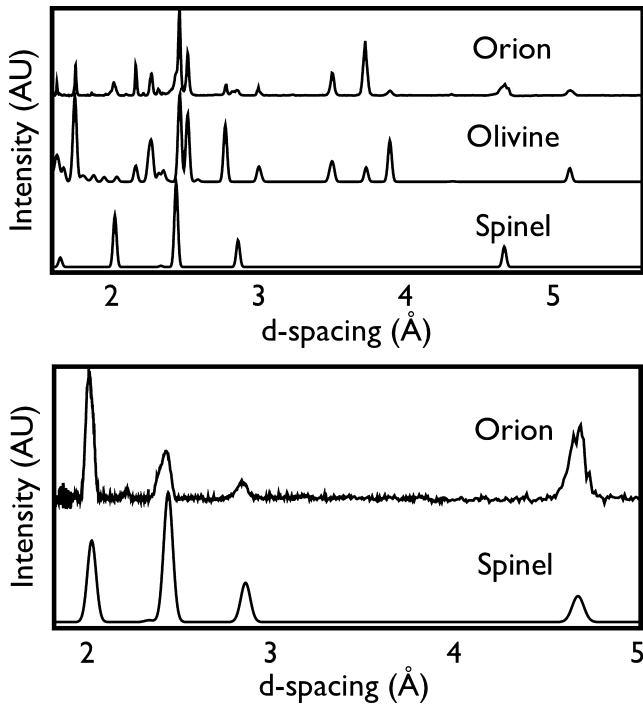


Fig. 8. The top panel compares the 1D powder integration from the ID13 SD image for Orion with model spectra for olivine and spinel. The 2-D pattern was processed to remove bad pixel instrumental artifacts showing as false peaks before integrating. The bottom panel compares the 1D powder integration pattern from the ID22 SD image for Orion with a model spectrum for spinel.

Butterworth et al. 2014), so we considered the possibility of Fe metal and sulfide phases. Kamacite, the most common room temperature structure of pure Fe metal, has an 011 reflection at 2.02 Å. We produced a topograph of the 2.02 Å d-spacing and found a phase appearing as a shell around the olivine. Additionally, the FWHM of the 2.02 Å reflection was nearly double the FWHM of nearby reflections, which pointed to phase which was either highly strained or nanoparticulate. With further investigation we found that the 2.434 Å spinel peak had a topograph that overlapped 2.02 Å topograph in some areas. They were not identical, however, so it may have had a contribution from another phase. We named the 2.02 Å topograph the unknown shell phase to reflect this uncertainty. Regardless, if the olivine were wrapped in a polycrystalline material, or an amorphous material with nanocrystalline inclusions, then the topograph should have appeared as it does in Fig. 9D, viz. a 2D projection of a hollow cylinder or ellipsoid.

Synthesizing the topographs from Figs. 9 and 10, it is clear that the center of Orion was olivine and spinel appeared on each end. The unknown shell phase was most intense around the rim of the olivine. The

Table 6. Measured and model peak positions for phases in Orion.

$d_{\text{meas}}^a$	$d_{\text{model}}^b$	FWHM	$hkl_{\text{fo}}$	$hkl_{\text{sp}}$
8.844		0.207		
5.116	5.113	0.092	020	
4.663	4.668	0.164		111
4.309	4.317	0.051	110	
3.888	3.890	0.129	021	
3.721	3.729	0.129	101	
3.498	<b>3.503</b>	0.141	111	
	3.485		120	
3.229		*c		
3.167		*		
2.996	3.013	0.165	121	
	<b>2.997</b>		002	
2.841	2.858	0.368		022
2.775	2.772	0.138	130	
n.d.	2.586	n.d.	022	
n.d.	2.556	n.d.	040	
2.515	2.516	0.200	131	
2.459	2.462	0.189	112	
2.434	2.438	0.242		113
n.d.	2.381	n.d.	200	
2.351	2.351	0.116	041	
n.d.	2.334	n.d.		222
2.317	2.319	0.182	210	
2.267	<b>2.272</b>	0.267	122	
	2.252		140	
2.215		0.127		
2.163	<b>2.163</b>	0.178	211	
	2.158		220	
2.097	2.108	0.208	141	
2.015	2.035	0.420	132	
	2.031		221	
	<b>2.021</b>			004

<sup>a</sup>Centroids of the experimentally measured peaks for Orion.

<sup>b</sup>Centroids expected from  $\text{Fo}_{100}$  or spinel. Where the experimental pattern was unable to resolve close reflections, two model peaks are assigned. In this case bold text indicates a peak is far more intense than the others at the same d-spacing. Spinel peaks are also italicized to distinguish them from olivine.

<sup>c</sup>The peak position was too weak in the radial integration to determine a FWHM.

unknown core phase was at one end, slightly to the side. Orion was a heterogeneous object because the olivine, spinel, and the unknown phases were segregated spatially.

### Olivine Analysis

All olivine reflections are shown in Table 5. We computed the Smith-Snyder figure of merit,  $F_N$  (Smith and Snyder 1979) in the same fashion as for Hylabrook and found that  $F_{13} = 51$  for the raw data when fit to  $\text{Fo}_{100}$ , and  $F_{13} = 110$  after removing any systematic error due to camera length calibration. In this case, the

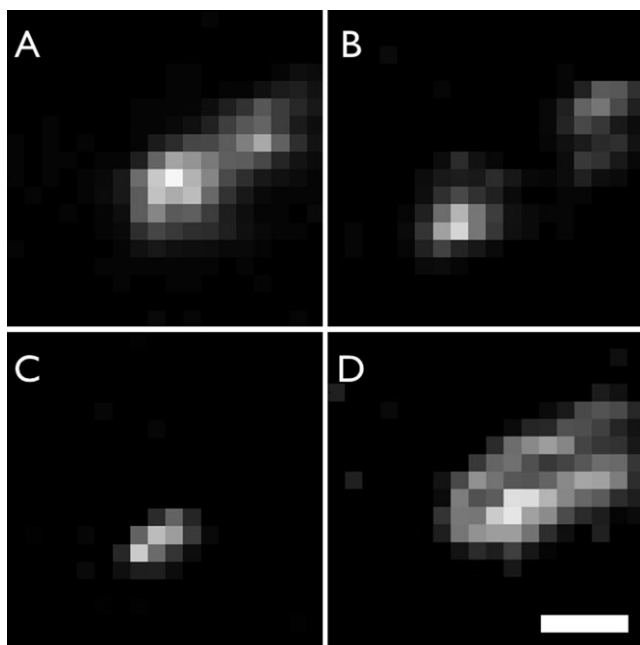


Fig. 9. A) Topograph generated from 30 reflections of olivine showing the position of the olivine phase in Orion. B) Topograph generated from the two longest d-spacings of spinel showing the spinel phase in Orion/Sirus. C) Topograph generated from the d-spacing at 8.84 Å corresponding to an unknown phase. D) Topograph generated from the 2.02 Å reflection, which contains olivine, spinel, and a third phase. 1  $\mu\text{m}$  scalebar.

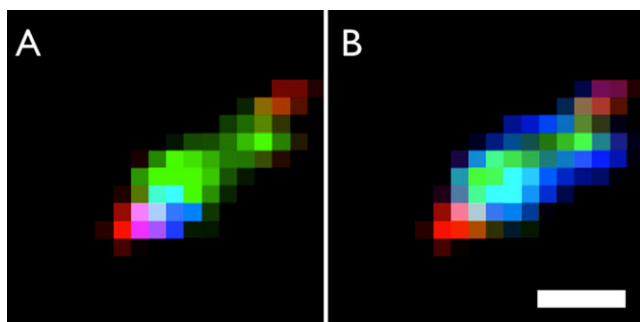


Fig. 10. A) Composite RGB image of spinel (red), olivine (green), and an unknown phase (blue). Olivine is the mineral at the core of Orion, while spinel appears to occupy the two ends, along with the unknown phase at one end. B) RGB image of spinel (red), olivine (green), and the olivine+spinel+third phase (blue). Because there are pixels which are intense in the blue, but not the red or green, we conclude that despite contamination from the olivine and spinel reflections, there must be a third diffracting phase, which appears to be more intense around the periphery of the olivine. 1  $\mu\text{m}$  scalebar.

reflection at 2.015 Å has been excluded because it overlapped spinel and shell phase peaks, and the peak at 2.097 was not counted in  $F_N$  because its intensity was

Table 7. Computed unit cell parameters with error bars for Orion olivine.

Parameter	Value	$\pm 2\sigma$ abs	$\pm 2\sigma$ rel
a	4.76	0.05	1%
b	10.23	0.10	1%
c	5.99	0.06	1%
a/b	0.465	0.0014	0.3%
a/c	0.795	0.0028	0.4%
V	291	8	3%

only 0.001% of the strongest line. Similarly to Hylabrook, we fit our 80 fingerprints and found that only olivine group minerals fit all the peaks seen and still maintained a high  $F_N$ . To measure the unit cell, we applied the same Monte Carlo approach used for Hylabrook with 50,000 trials:  $a = 4.76 \pm 0.05$  Å,  $b = 10.23 \pm 0.10$  Å,  $c = 5.99 \pm 0.06$  Å where all error bars are  $2\sigma$  (Table 7). Figure 11 shows the distribution of values computed by the Monte Carlo. The detector geometry calibration for Orion was of higher quality than it was for Hylabrook. As a result, the nonsystematic variation was only 0.2% rather than 1% for Hylabrook. The systematic error (camera length calibration) remained at 1% as it was for Hylabrook. The distributions for the unit cell parameters a, b, and c and volume had a boxcar shape. Shown in Fig. 11 the boxcars reflect the fact that all unit cell parameters could be systematically altered by 1%, but were well known relative to each other. The ratios a/b and a/c, which were essentially independent of the systematic error, remained much closer to normal distributions.

In contrast with Hylabrook, we had enough accuracy in the unit cell measurement to examine chemical composition. The unit cell of olivine varies with cation concentration and the cation radius (Fisher and Medaris 1969; Lumpkin and Ribbe 1983; Koch et al. 2004). Using Lumpkin and Ribbe (1983) and a Monte Carlo code we wrote in MATLAB<sup>®</sup>, we computed the radius of the tetrahedral cation to be  $0.28 \pm 0.08$  Å (Fig. 12A). Si and Be are the only known cations in this range of radii within olivine structure minerals. Likewise, Fig. 12B shows the M1 site radius to be  $0.75 \pm 0.08$  Å. For comparison, Mg is 0.72, Fe is 0.78 Å, and Ca is 1.00 Å. As M1 and M2 cations in the beryllonates have radii of 0.54 – 0.62 Å, we ruled this out and claimed that Si was the tetrahedral cation. To compute the M1/M2 ratio, we took advantage of the fact that the ratios of the unit cell parameters a/b and a/c were better known than the absolute values for a, b, and c. Figures 12C and 12D show computed results using the ratioed unit cell and assuming silicon for the tetrahedral cation. M1/M2 is tightly constrained between 0.96 and 1.00

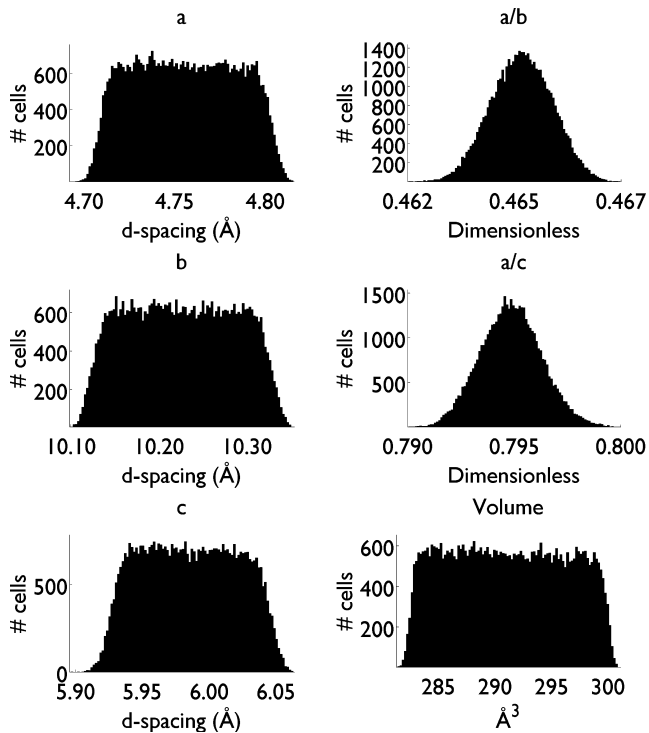


Fig. 11. Error distributions for the unit cell parameters of olivine in Orion.

(Fig. 12C). The M1 site is between 0.71 and 0.75 Å. Pure forsterite is entirely consistent with these results. Pure fayalite is inconsistent. Because the M1/M2 ratio is close to 1, the size of the cations in M1 and M2 must be similar. In olivines with large and small cations, the larger cations take the M2 site leading to a reduction in M1/M2 from 1. Therefore, our optimal choice for a composition comes from the centroids of our error distributions: M1/M2 = 0.98 and M1 = 0.73 Å, which matches  $\approx$  Fo<sub>85</sub>. Other olivines are consistent within our error bars. For example, (Mg<sub>1.91</sub>Ca<sub>0.09</sub>)SiO<sub>4</sub> has M1 = 0.72, and an M1/M2 = 0.97 while Fo<sub>71</sub> has M1 = 0.74, and M1/M2 = 1. Therefore, the 2 $\sigma$  upper limits for binary compositions are: fayalite <35 molar%, calcio-olivine <5%, and tephroite (Mn) <25%.

A size-strain analysis was less useful in the case of Orion compared with Hylabrook because the average image was significantly less intense than Hylabrook's. The fits to the peak shapes were correspondingly noisier, although the centroids were still well determined. For this reason, the error bars on the size-strain analysis were too large to be very useful, but nevertheless, we found little evidence for size broadening of the olivine peaks and the 2 $\sigma$  lower limit on the olivine domain size was 27 nm. Strain within the olivine was limited to  $\leq$  1%. The olivine domain sizes

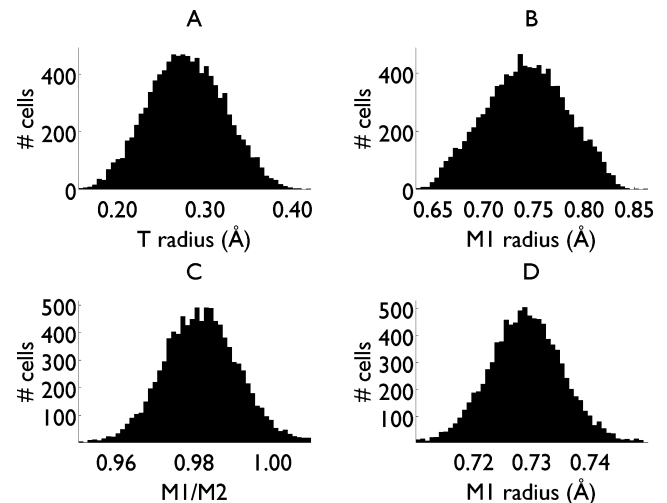


Fig. 12. Error distributions for the computed atomic site radii in Orion olivine. A shows the radius of the tetrahedral site usually occupied by silicon (0.260 Å). B shows the size of the M1 site (Mg = 0.72, Fe = 0.78). C shows the ratio of M1/M2 after removing errors due to camera length calibration, and assuming the tetrahedral cation is Si. D shows the M1 computation after removing errors and assuming tetrahedral Si.

were better elucidated by the topographical analysis, as many olivine domains were larger than the pixel size and could be resolved in real space.

### Olivine Mosaicism

The topographs showed that the olivine was heavily mosaiced. Figure 13 shows a mosaic with an asterism of about 20°. Topographs produced from eight positions along the asterism are shown in juxtaposition and labeled by their azimuthal coordinate,  $\chi$ , defined as the counterclockwise azimuthal angle from 3 o'clock in the diffraction image. The point spread function blurred the topograph view of the mosaic domains slightly, so we may consider each of the topographs to be approximately 1 pixel too large on each face. Given this correction, the largest mosaic domain was 1.2  $\mu$ m long. The domains overlapped significantly and reflections chosen in a counterclockwise direction along the debye ring correlated with domains progressively down and to the left in the topograph images. Based on this evidence, this olivine was a dense object and not exclusively polycrystalline. If it were polycrystalline, then we should expect no correlation between the azimuthal position of a domain's reflection and its spatial orientation. We can investigate the maximum angle between the mosaiced domains using the azimuthal broadening in the 2D XRD pattern. Per Cullity and Stock (1978),

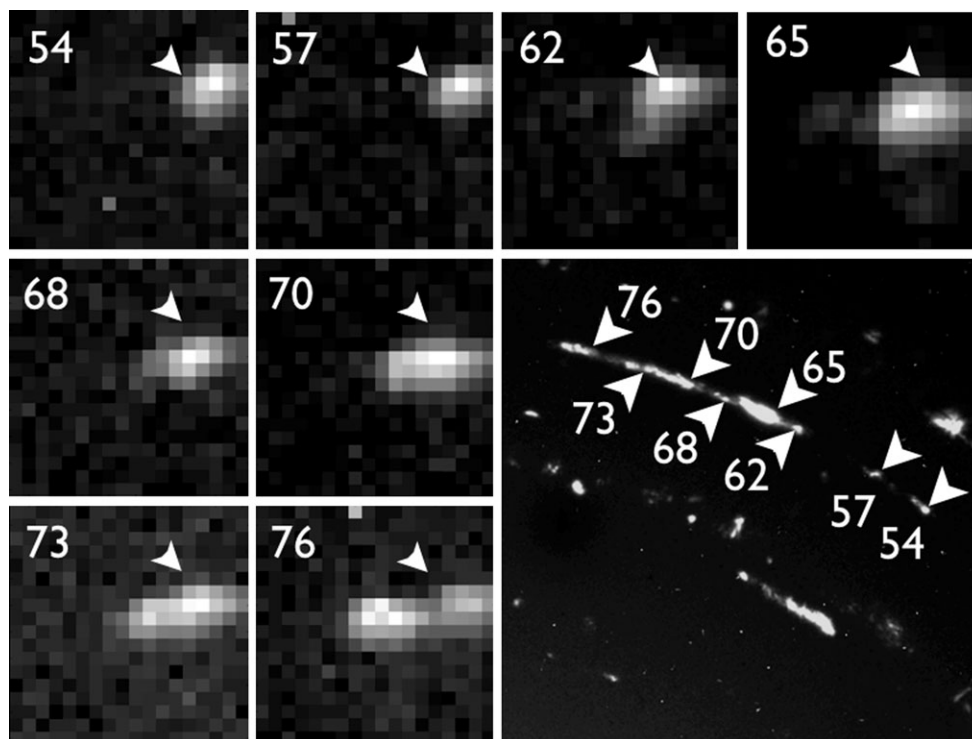


Fig. 13. A mosaiced olivine reflection at  $2.16 \text{ \AA}$  (lower right image) corresponds to the 211 or 220 reflection of olivine. The numbered images are topographs where the number represents the azimuthal position ( $\chi$ ) in the diffraction pattern showing that this mosaic spread occurs over approximately  $20^\circ$  in azimuth. A fixed coordinate is marked in all topographs to clarify the fact that different real-space domains are responsible for the reflections. The topograph pixel sizes are  $190 \text{ nm}$ . The mosaic extends almost two microns in real space.

$$\phi = 2 \varepsilon \tan(2\theta) \quad (3)$$

where  $\phi$  is the azimuthal broadening, and  $\varepsilon$  is the variation in the angle of the diffractive domains (mosaicity). For this reflection at  $2.16 \text{ \AA}$  ( $2\theta = 23.8^\circ$ ), we obtained  $\varepsilon = 23^\circ$ . This variation was clearly too large to be due to internal strain or size broadening and so was due to grain boundaries or disconnected grains.

Conversely, a smaller number of tiny olivine domains were also visible such as the one shown in Fig. 2. These were essentially single pixel reflections, blurred only by the PSF of the beamline. They did not have an obvious orientation to other crystallites, and so it appears that polycrystalline olivine was also present. We have an upper limit of  $400 \text{ nm}$  from the topographs for the size of the polycrystalline domains. Therefore, the mosaic crystal should account for the bulk of the olivine mass as it would require a large number of the polycrystallites to equal the volume of the mosaic seen in Fig. 13.

If we assume that the olivine was compact, then we can make an order of magnitude estimate of its size by approximating the shape seen in the sum topograph (Fig. 9A) as an ellipsoid with volume  $V = (4\pi/3)abc$  where  $a$ ,  $b$ ,

and  $c$  are the three radii of the ellipsoid. Because of the point spread function of the topographs (Fig. 2), we should remove one pixel from the side of each topograph, and then we can determine two radii of the olivine as  $1.1$  and  $0.3 \text{ \mu m}$ . If we assume that the depth dimension was equal to the smallest lateral dimension ( $0.3 \text{ \mu m}$  radius), then the volume of the ellipsoid was  $0.41 \text{ \mu m}^3$ . Using the density for forsterite of  $3.25 \text{ g cm}^{-3}$ , this gave a total olivine mass of  $1300 \text{ fg}$ , and a total Mg mass of  $460 \text{ fg}$ . The STXM results estimated  $\approx 1 \text{ pg}$  of forsterite (Butterworth et al. 2014), which is in good agreement considering we cannot know exactly how well the ellipsoid approximation represented the actual particle.

### Spinel Analysis

We previously calculated an  $8.06 \text{ \AA}$  cubic unit cell from from the four brightest nonolivine reflections in ID13. Again, we applied our Monte Carlo routines to obtain error bars for the unit cell dimensions. Cubic symmetry requires  $a = b = c$  and  $\alpha = \beta = \gamma = 90^\circ$ . The resulting unit cell had a dimension:  $a = 8.06 \pm 0.08 \text{ \AA}$  ( $2\sigma$ ). The figure of merit for spinel was  $F_4 = 28$  for the raw data and  $F_4 = 57$  after removing any

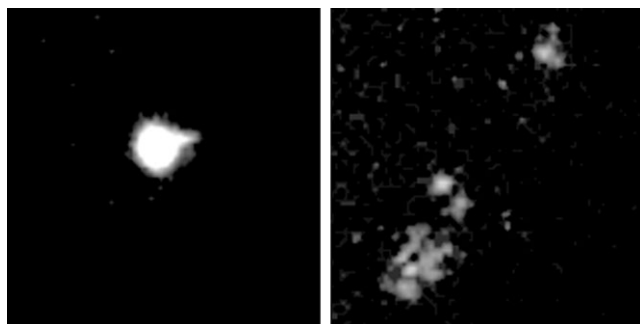


Fig. 14. Two reflections produced by the longest d-spacing in spinel: 4.66 Å (111).

camera length calibration error. A size-strain analysis was difficult for the spinel as only the two longest (highest d-spacing) peaks were clearly separated from the olivine peaks. The reflections were so sparsely populated that it was not possible to get a good quantitative understanding of the spreading, although we observed distinct crystallites with variable spreading, either due to crystallite size, strain, or both. Figure 14 shows images for two reflections from the longest spinel d-spacing, 4.66 Å. Whereas one appeared as a nearly perfect crystal, the other was barely discernable as the asterism was so great. Therefore, the characteristics of the spinel crystals were highly inhomogeneous.

The spinel topographs did not appear to bear the same mosaicity relationship seen in the olivine. Figure 15 shows topographs for all the peaks at the longest d-spacing for spinel, 4.66 Å corresponding to the 111 reflection. There appeared to be a sequence of closely spaced peaks with an azimuthal spread of 20° going from  $\chi = 34^\circ$  to  $54^\circ$ . However, the topographs showed that the peaks mapped to crystallites on opposite sides of the olivine grain and did not show a clear mosaicity or polygonalization. There may still have been some relationship, for example, the topographs for  $\chi = 34^\circ$ ,  $41^\circ$ , and  $48^\circ$  appear to be close, but it is also important to note that each of these topographs is essentially the PSF for the beamline so there is no guarantee that the grains were large enough to overlap. One reasonable explanation is that the grains were nanocrystals within a volume of amorphous material.

### Fitting Unknown Phases

We know from XRF analysis (Brenker et al. 2014) that significant iron and sulfur were present in the particle, and that these were among the most mobile elements during synchrotron irradiation. Additionally, carbon was invisible to XRF and STXM due to experimental limitations so we also considered whether Fe, sulfide, or carbonaceous materials could fit either of the unknown phases.

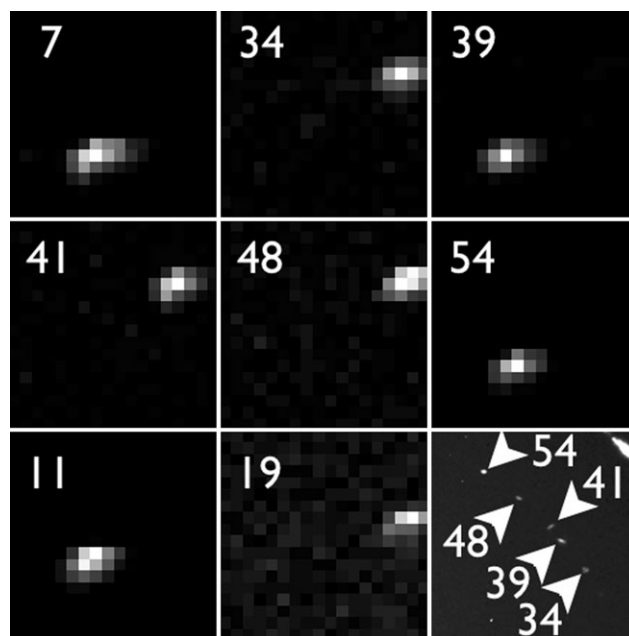


Fig. 15. Topographs for all the 4.66 Å spinel reflections. The number in each box represents the azimuthal position in the diffraction pattern ( $\chi$ ). Lower-right inset is a cluster of reflections with an azimuthal spread over 20°.

We might expect to have seen nanoparticulate Fe from glass with embedded metal and sulfides (Bradley 2007), space weathering of olivine (Hapke 2001), or aerogel capture of sulfides (Leroux et al. 2009). If nanoparticulate Fe were present, it would have shown as the 2.02 Å reflection such as in the shell phase. However, nano-Fe could not have made the 2.434 Å reflection. There are no iron sulfides with both these reflections dominating others, although pyrite can make the 2.434 Å reflection. We should note that known spinel-sulfide phases such as those found in IDPs (Dai and Bradley 2001) and greigite probably did not produce these reflections since their unit cell is too large. Because sulfides readily decompose upon aerogel capture into an Fe-metal core and Fe sulfide rim (Leroux et al. 2009), it follows that absence of a sulfide signature does not rule out the presence of sulfides prior to the collection. However, the presence of S in the XRF could be explained if sulfides present in the incident particle decomposed due to aerogel capture in the same fashion as we see in the cometary samples (Leroux et al. 2009). We would expect a residual nano-Fe core, which would show up as a 2.02 Å ring and the sulfur would remain in amorphous phases invisible to the XRD.

Graphite could also produce the 2.02 Å reflection, but should produce a 3.36 Å reflection as well that we did not see, so we conclude that graphite was

not abundant. We did note that the 8.844 Å reflection could be produced by intercalated graphite-nitrates (Nixon et al. 1966), although it seemed difficult to justify these in an extraterrestrial environment. Theoretical calculations and experiment have shown a number of stable intermediates between graphite and diamond including orthorhombic structures, rhombohedral, etc. (Blank et al. 1999; Fayos 1999) so it is not inconceivable that some of the diffractions in the two unknown phases are due to carbonaceous materials. We also tried silicon carbide polytypes 2H and 3C, and diamond but these failed to provide a satisfactory fit.

### Summary of Orion

Combining the evidence above, Orion was originally a mosaiced olivine grain about  $2.2 \times 0.6 \mu\text{m}$  alongside nanocrystalline olivines and nanocrystalline spinel. Two other unknown phases were also present intermixed or adjacent to the olivine and spinel. Amorphous carbonaceous or silicate material may have been present, nanoparticles of any sort (e.g., nanodiamonds, etc.) may have been present in low volume abundance and were not detected. To the nearest order of magnitude, there was about 1 pg of crystalline olivine present and the composition was  $> \text{Fo}_{65}$  ( $2\sigma$ ). The olivine unit cell was  $a = 4.76 \pm 0.05 \text{ \AA}$ ,  $b = 10.23 \pm 0.10 \text{ \AA}$ ,  $c = 5.99 \pm 0.06 \text{ \AA}$  ( $2\sigma$ ) with strain  $<1\%$  averaged. The spinel was nanocrystalline with all nanocrystals  $<400 \text{ nm}$  in lateral extent. The unit cell was cubic with  $a = 8.06 \pm 0.08 \text{ \AA}$  ( $2\sigma$ ). The crystal quality differed greatly between individual spinels and olivines.

### CONCLUSIONS

X-ray diffraction measurements have revealed that two interstellar dust candidates identified during the Stardust ISPE had a significant crystalline fraction. The first, track 34 (Hylabrook), was an olivine grain several hundred nanometers across and manifested asterism of several degrees due to mosaicity and microstrain fields up to 0.3%. The second, track 30 (Orion), was a multicrystalline object consisting of a polycrystalline olivine core approximately  $2.2 \mu\text{m}$  long with attached polycrystalline spinel and at least two additional phases. In Orion, the olivine had both mosaic and polycrystalline characters, and microstrain fields up to 1%. The unit cell dimensions restricted the composition to relatively forsteritic values, with a  $2\sigma$  composition of  $\text{Fo}_{65}$  or higher. The spinel grains were all  $<400 \text{ nm}$  across, and probably much smaller. We could not set any compositional constraints on the spinel from the diffraction information. Both Orion and Hylabrook may

have had significant organic and inorganic amorphous components that we did not see in diffraction.

*Acknowledgments*—Zack Gainsforth, Andrew J. Westphal, Anna L. Butterworth were supported by NASA grant NNX09AC36G. The operations of the Advanced Light Source at Lawrence Berkeley National Laboratory are supported by the Director, Office of Science, Office of Basic Energy Sciences, U.S. Department of Energy under contract number DE-AC02-05CH11231.

We thank the NASA Discovery Mission program for providing a cost-effective and highly productive sample return mission, and believe that the Stardust mission provided a most valuable precedent for future sample return excursions throughout our solar system. We would like to thank the referees Conel Alexander and Michel Maurette for their productive review of this work.

*Editorial Handling*—Dr. Christian Koeberl

### REFERENCES

- Abramson E., Brown J., Slutsky L., and Zaug J. 1997. The elastic constants of San Carlos olivine to 17 GPa. *Journal of Geophysical Research-Solid Earth* 102:12253–12263.
- Adler T. and Houska C. 1979. Simplifications in the X-ray line-shape analysis. *Journal of Applied Physics* 50:3282–3287.
- Anderson W. W. 1998. Physics of interplanetary dust collection with aerogel. NASA STI/Recon Technical Report NASACR-1998-207766. pp. 1–24.
- Balzar D. 1999. Voigt-function model in diffraction line-broadening analysis. *International Union of Crystallography Monographs on Crystallography* 10:94–126.
- Black D. and Long G. 2004. *X-ray topography, SP 960-10*. Washington, D.C.: US Government Printing Office.
- Blank V. D., Aksenkov V. V., Popov M. Y., Perfilov S. A., Kulnitskiy B. A., Tatyannin Y. V., Zhigalina O. M., Mavrin B. N., Denisov V. N., Ivlev A. N., Chernov V. M., and Stepanov V. A. 1999. A new carbon structure formed at MeV neutron irradiation of diamond: Structural and spectroscopic investigations. *Diamond and Related Materials* 8:1285–1290, doi:10.1016/S0925-9635(99)00118-1.
- Bleuet P., Simionovici A. S., Lemelle L., Ferroir T., Cloetens P., Tucoulou R., and Susini J. 2008. Hard x-rays nanoscale fluorescence imaging of Earth and planetary science samples. *Applied Physics Letters* 92:213111, doi:10.1063/1.2927476.
- Bradley J. P. 2007. Interplanetary dust particles. In *Meteorites, comets, and planets*, edited by Davis A. M. Treatise on Geochemistry, vol. 1. Oxford: Pergamon. pp. 689–711.
- Brenker F. E., Schoonjans T., Silversmit G., Vekemans B., Vincze L., Westphal A. J., Allen C., Anderson D., Ansari A., Bajt S., Bastien R. K., Bassim N., Bechtel H. A., Borg J., Bridges J., Brownlee D. E., Burchell M., Burghammer M., Butterworth A. L., Changela H., Cloetens P., Davis A. M., Doll R., Floss C., Flynn G., Fougerey P., Frank D. R.,

- Gainsforth Z., Grün E., Heck P. R., Hillier J. K., Hoppe P., Hudson B., Huss G., Huth J., Hvide B., Kearsley A.-t., King A. J., Lai B., Leitner J., Lemelle L., Leroux H., Leonard A., Lettieri R., Marchant W., Nittler L. R., Ogliore R., Ong W. J., Postberg F., Price M. C., Sandford S. A., Tresseras J.-A. S., Schmitz S., Simionovici A. S., Solé V. A., Srama R., Stephan T., Sterken V. J., Stodolna J., Stroud R. M., Sutton S., Trieloff M., Tsou P., Tsuchiyama A., Tylliszczak T., Von Korff J., Wordsworth N., Zevin D., Zolensky M. E., and >30,000 Stardust@home dusters. 2014. Stardust Interstellar Preliminary Examination VII: XRF analyses of interstellar dust candidates at ESRF ID13. *Meteoritics & Planetary Science*, doi:10.1111/maps.12206.
- Brownlee D., Tsou P., Aléon J., Alexander C. M. O., Araki T., Bajt S., Baratta G. A., Bastien R. K., Bland P., Bleuett P., Borg J., Bradley J. P., Brearley A., Brenker F., Brennan S., Bridges J. C., Browning N. D., Brucato J. R., Bullock E., Burchell M. J., Busemann H., Butterworth A. L., Chaussidon M., Chevront A., Chi M., Cintala M. J., Clark B. C., Clemett S. J., Cody G., Colangeli L., Cooper G., Cordier P., Daghljan C., Dai Z. R., D'Hendecourt L., Djouadi Z., Dominguez G., Duxbury T., Dworkin J. P., Ebel D. S., Economou T. E., Fakra S., Fairey S. A. J., Fallon S., Ferrini G., Ferroir T., Fleckenstein H., Floss C., Flynn G. J., Franchi I. A., Fries M., Gainsforth Z., Gallien J.-P., Genge M., Gilles M. K., Gillet P., Gilmour J., Glavin D. P., Gounelle M., Grady M. M., Graham G. A., Grant P. G., Green S. F., Grossemy F., Grossman L., Grossman J. N., Guan Y., Hagiya K., Harvey R., Heck P., Herzog G. F., Hoppe P., Hoerz F., Huth J., Hutcheon I. D., Ignatyev K., Ishii H., Ito M., Jacob D., Jacobsen C., Jacobsen S., Jones S., Joswiak D., Jurewicz A., Kearsley A. T., Keller L. P., Khodja H., Kilcoyne A. L. D., Kissel J., Krot A., Langenhorst F., Lanzirrotti A., Le L., Leshin L. A., Leitner J., Lemelle L., Leroux H., Liu M.-C., Luening K., Lyon I., MacPherson G., Marcus M. A., Marhas K., Marty B., Matrajt G., McKeegan K., Meibom A., Mennella V., Messenger K., Messenger S., Mikouchi T., Mostefaoui S., Nakamura T., Nakano T., Newville M., Nittler L. R., Ohnishi I., Ohsumi K., Okudaira K., Papanastassiou D. A., Palma R., Palumbo M. E., Pepin R. O., Perkins D., Perronnet M., Pianetta P., Rao W., Rietmeijer F. J. M., Robert F., Rost D., Rotundi A., Ryan R., Sandford S. A., Schwandt C. S., See T. H., Schlutter D., Sheffield-Parker J., Simionovici A. S., Simon S., Sitnitsky I., Snead C. J., Spencer M. K., Stadermann F. J., Steele A., Stephan T., Stroud R., Susini J., Sutton S. R., Suzuki Y., Taheri M., Taylor S., Teslich N., Tomeoka K., Tomioka N., Toppani A., Trigo-Rodríguez J. M., Troadec D., Tsuchiyama A., Tuzzolino A. J., Tylliszczak T., Uesugi K., Velbel M., Vellenga J., Vicenzi E., Vincze L., Warren J., Weber I., Weisberg M., Westphal A. J., Wirick S., Wooden D., Wopenka B., Wozniakiewicz P., Wright I., Yabuta H., Yano H., Young E. D., Zare R. N., Zega T., Ziegler K., Zimmerman L., Zinner E., and Zolensky M. E. 2006. Comet 81P/Wild 2 under a microscope. *Science* 314:1711–1716, doi:10.1126/science.1135840.
- Brownlee D. E. 2003. Stardust: Comet and interstellar dust sample return mission. *Journal of Geophysical Research* 108:1811, doi:10.1029/2003JE002087.
- Burchell M. J., Cole M. J., Price M. C., and Kearsley A. T. 2012. Experimental investigation of impacts by solar cell secondary ejecta on silica aerogel and aluminum foil: Implications for the Stardust Interstellar Dust Collector. *Meteoritics & Planetary Science* 47:671–683. doi:10.1111/j.1945-5100.2011.01294.x.
- Butterworth A. L., Westphal A. J., Tylliszczak T., Gainsforth Z., Stodolna J., Frank D. R., Allen C., Anderson D., Ansari A., Bajt S., Bastien R. K., Bassim N., Bechtel H. A., Borg J., Brenker F. E., Bridges J., Brownlee D. E., Burchell M., Burghammer M., Changela H., Cloetens P., Davis A. M., Doll R., Floss C., Flynn G., Grün E., Heck P. R., Hillier J. K., Hoppe P., Hudson B., Huth J., Hvide B., Kearsley A., King A. J., Lai B., Leitner J., Lemelle L., Leroux H., Leonard A., Lettieri R., Marchant W., Nittler L. R., Ogliore R., Ong W. J., Postberg F., Price M. C., Sandford S. A., Tresseras J.-A. S., Schmitz S., Schoonjans T., Silversmit G., Simionovici A. S., Solé V. A., Srama R., Stephan T., Sterken V. J., Stroud R. M., Sutton S., Trieloff M., Tsou P., Tsuchiyama A., Vekemans B., Vincze L., Von Korff J., Wordsworth N., Zevin D., Zolensky M. E., and >30,000 Stardust@home dusters. 2014. X-ray absorption analyses of major rock-forming elements in candidate interstellar dust impacts by scanning transmission X-ray microscopy. *Meteoritics & Planetary Science*, doi:10.1111/maps.12220.
- CrystalMaker Software Ltd. 2012. *CrystalDiffract® version 5.2*. Oxfordshire, U.K.: CrystalMaker Software.
- Cullity B. and Stock S. 1978. *Elements of X-ray diffraction*, 2nd edition. Reading, Massachusetts: Addison-Wesley Publishing Company.
- Dai Z. and Bradley J. 2001. Iron-nickel sulfides in anhydrous interplanetary dust particles. *Geochimica et Cosmochimica Acta* 65:3601–3612.
- Fayos J. 1999. Possible 3D carbon structures as progressive intermediates in graphite to diamond phase transition. *Journal of Solid State Chemistry* 148:278–285.
- Fisher G. W. and Medaris L. G. 1969. Cell dimensions and X-ray determinative curve for synthetic Mg-Fe olivines. *The American Mineralogist* 54:741–753.
- Frank D. R., Westphal A. J., Zolensky M. E., Gainsforth Z., Butterworth A. L., Bastien R. K., Allen C., Anderson D., Ansari A., Bajt S., Bassim N., Bechtel H. A., Borg J., Brenker F. E., Bridges J., Brownlee D. E., Burchell M., Burghammer M., Changela H., Cloetens P., Davis A. M., Doll R., Floss C., Flynn G., Grün E., Heck P. R., Hillier J. K., Hoppe P., Hudson B., Huth J., Hvide B., Kearsley A., King A. J., Lai B., Leitner J., Lemelle L., Leroux H., Leonard A., Lettieri R., Marchant W., Nittler L. R., Ogliore R., Ong W. J., Postberg F., Price M. C., Sandford S. A., Tresseras J.-A. S., Schmitz S., Schoonjans T., Silversmit G., Simionovici A. S., Solé V. A., Srama R., Stephan T., Sterken V. J., Stodolna J., Stroud R. M., Sutton S., Trieloff M., Tsou P., Tsuchiyama A., Tylliszczak T., Vekemans B., Vincze L., Von Korff J., Wordsworth N., Zevin D., and >30,000 Stardust@home dusters. 2013. Stardust Interstellar Preliminary Examination II: Curating the interstellar dust collector, picokeystones, and sources of impact tracks. *Meteoritics & Planetary Science* 48, doi:10.1111/maps.12147.
- Grün E., Zook H., Baguhl M., Balogh A., Bame S. J., Fechtig H., Forsyth R., Hanner M., Horanyi M., Kissel J., Lindblad B. A., Linkert D., Linkert G., Mann I., McDonnell J. A. M., Morfill G., Phillips J., Polansky C., Schwehm G., Siddique N., Staubach P., Svestka J., and

- Taylor A. 1993. Discovery of Jovian dust streams and interstellar grains by the Ulysses spacecraft. *Nature* 362:428–430.
- Hapke B. 2001. Space weathering from Mercury to the asteroid belt. *Journal of Geophysical Research* 106:10039–10074, doi:10.1029/2000JE001338.
- International Center for Diffraction Data. 2012. *PDF-4+/Minerals*. Newtown Square, Pennsylvania: International Center for Diffraction Data.
- Kemper F., Vriend W. J., and Tielens A. G. G. M. 2004. The absence of crystalline silicates. *The Astrophysical Journal* 609:826–837, doi:10.1086/421339.
- Kemper F., Vriend W. J., and Tielens A. G. G. M. 2005. Erratum: “The Absence of Crystalline Silicates in the Diffuse Interstellar Medium” (*ApJ*, 609, 826 [2004]). *The Astrophysical Journal* 633:534–534, doi:10.1086/447764.
- Kim S.-H., Martin P. G., and Hendry P. D. 1994. The size distribution of interstellar dust particles as determined from extinction. *The Astrophysical Journal* 422:164–175, doi:10.1086/173714.
- Koch M., Woodland A. B., and Angel R. J. 2004. Stability of spineloid phases in the system  $Mg_2SiO_4$ - $Fe_2SiO_4$ - $Fe_3O_4$  at 1100°C and up to 10.5 GPa. *Physics of the Earth and Planetary Interiors* 143:171–183, doi: 10.1016/j.pepi.2003.06.001.
- Lagarias J., Reeds J., Wright M., and Wright P. 1998. Convergence properties of the Nelder-Mead simplex method in low dimensions. *Siam Journal on Optimization* 9:112–147.
- Le Bail A. 2004. Monte Carlo indexing with McMaille. *Powder Diffraction* 19:249–254, doi:10.1154/1.1763152.
- Leroux H., Roskosz M., and Jacob D. 2009. Oxidation state of iron and extensive redistribution of sulfur in thermally modified Stardust particles. *Geochimica et Cosmochimica Acta* 73:767–777, doi:10.1016/j.gca.2008.09.037.
- Lodders K. and Amari S. 2005. Presolar grains from meteorites: Remnants from the early times of the solar system. *Chemie der Erde-Geochemistry* 65:93–166.
- Lumpkin G. R. and Ribbe P. H. 1983. Composition, order-disorder and lattice parameters of olivines: Relationships in silicate germanate, beryllate, phosphate, and borate olivines. *American Mineralogist* 68:164–176.
- MathWorks, Inc. 2011. MATLAB® Version R. Natick, Massachusetts: MathWorks, Inc.
- Nixon D. E., Parry G. S., and Ubbelohde A. R. 1966. Order-disorder transformations in graphite nitrates. *Proceedings of the Royal Society of London A* 291:324–339, doi:10.1098/rspa.1966.0098.
- Pendleton Y., Sandford S. A., Allamandola L., Tielens A., and Sellgren K. 1994. Near-infrared absorption spectroscopy of interstellar hydrocarbon grains. *The Astrophysical Journal* 437:683–696.
- Postberg F., Hillier J. K., Armes S. P., Bugiel S., Butterworth A. L., Dupin D., Fielding L. A., Fujii S., Gainsforth Z., Grün E., Li Y. W., Srama R., Sterken V. J., Stodolna J., Trieloff M., Westphal A. J., Achilles C., Allen C., Ansari A., Bajt S., Bassim N., Bastien R. K., Bechtel H. A., Borg J., Brenker F., Bridges J., Brownlee D. E., Burchell M., Burghammer M., Changela H., Cloetens P., Davis A., Doll R., Floss C., Flynn G., Frank D. R., Heck P.R., Hoppe P., Huss G., Huth J., Kearsley A., King A. J., Lai B., Leitner J., Lemelle L., Leonard A., Leroux H., Lettieri R., Marchant W., Nittler L. R., Oglione R., Ong W. J., Price M. C., Sandford S. A., Tresseras J.-A. S., Schmitz S., Schoonjans T., Schreiber K., Silversmit G., Simionovici A. S., Solé V. A., Stephan T., Stodolna J., Stroud R. M., Sutton S., Trieloff M., Tsou P., Tsuchiyama A., Tyliczszak T., Vekemans B., Vincze L., Von Korff J., Wordsworth N., Zevin D., and Zolensky M. E. 2014. Impact speeds and
- S., Schoonjans T., Schreiber K., Silversmit G., Simionovici A. S., Solé V. A., Stadermann F., Stephan T., Stroud R. M., Sutton S., Tsou P., Tsuchiyama A., Tyliczszak T., Vekemans B., Vincze L., Zevin D., Zolensky M. E., and >30,000 Stardust@home dusters. 2014. Stardust Interstellar Preliminary Examination IX: High speed interstellar dust analogue capture in Stardust flight-spore aerogel. *Meteoritics & Planetary Science*, doi:10.1111/maps.12173.
- Sandford S. A., Allamandola L., Tielens A., Sellgren K., Tapia M., and Pendleton Y. 1991. The interstellar CH stretching band near 3.4 microns—Constraints on the composition of organic material in the diffuse interstellar medium. *The Astrophysical Journal* 371:607–620.
- Sandford S. A., Pendleton Y. J., and Allamandola L. J. 1995. The galactic distribution of aliphatic hydrocarbons in the diffuse interstellar medium. *The Astrophysical Journal* 440:1–10, doi:10.1086/175307.
- Scherrer P. 1918. Bestimmung der Grösse und der inneren Struktur von Kolloidteilchen mittels Röntgenstrahlen. *Nachrichten von der Gesellschaft Wissenschaften zu Göttingen* 26:98–100.
- Simionovici A. S., Lemelle L., Cloetens P., Solé V. A., Tresseras J.-A. S., Butterworth A. L., Westphal A. J., Gainsforth Z., Stodolna J., Allen C., Anderson D., Ansari A., Bajt S., Bassim N., Bastien R. K., Bechtel H. A., Borg J., Brenker F. E., Bridges J., Brownlee D. E., Burchell M., Burghammer M., Changela H., Davis A. M., Doll R., Floss C., Flynn G., Frank D. R., Grün E., Heck P. R., Hillier J. K., Hoppe P., Hudson B., Huth J., Hvide B., Kearsley A., King A. J., Lai B., Leitner J., Leonard A., Leroux H., Lettieri R., Marchant W., Nittler L. R., Oglione R., Ong W. J., Postberg F., Price M. C., Sandford S. A., Schmitz S., Schoonjans T., Schreiber K., Silversmit G., Srama R., Stephan T., Sterken V. J., Stroud R. M., Sutton S., Trieloff M., Tsou P., Tsuchiyama A., Tyliczszak T., Vekemans B., Vincze L., Von Korff J., Wordsworth N., Zevin D., Zolensky M. E., and >30,000 Stardust@home dusters. 2014. Stardust Interstellar Preliminary Examination VI: Quantitative elemental analysis by synchrotron X-ray fluorescence nanoimaging of eight impact features in aerogel. *Meteoritics & Planetary Science*, doi:10.1111/maps.12208.
- Smith G. and Snyder R. 1979. FN: A criterion for rating powder diffraction patterns and evaluating the reliability of powder-pattern indexing. *Journal of Applied Crystallography* 12:60–65.
- Sterken V. J., Westphal A. J., Altobelli N., n E. G., Postberg F., Srama R., Allen C., Anderson D., Ansari, A., Bajt S., Bastien, R. K., Bassim N., Bechtel H. A., Borg J., Brenker F. E., Bridges J., Brownlee D. E., Burchell M., Burghammer M., Butterworth A. L., Changela H., Cloetens P., Davis A. M., Doll R., Floss C., Flynn G., Fougeray P., Frank D. R., Gainsforth Z., Heck P. R., Hillier J. K., Hoppe P., Hudson B., Huss G., Huth J., Hvide B., Kearsley A., King A. J., Lai B., Leitner, J., Lemelle, L., Leroux H., Leonard A., Lettieri R., Marchant, W., Nittler L. R., Oglione R., Ong W. J., Price M. C., Sandford S. A., Tresseras J.-A. S., Schmitz S., Schoonjans T., Silversmit G., Simionovici A. S., Solé V. A., Stephan T., Stodolna J., Stroud R. M., Sutton S., Trieloff M., Tsou P., Tsuchiyama A., Tyliczszak T., Vekemans B., Vincze L., Von Korff J., Wordsworth N., Zevin D., and Zolensky M. E. 2014. Impact speeds and

- directions of interstellar grains on the Stardust dust collector. *Meteoritics & Planetary Science*, doi:10.1111/maps.12219.
- Stodolna J., Jacob D., Leroux H., and Burchell M. J. 2012. Microstructure modifications of silicates induced by the collection in aerogel: Experimental approach and comparison with Stardust results. *Meteoritics & Planetary Science* 46:696–707, doi:10.1111/j.1945-5100.2011.01305.x.
- Stokes A. and Wilson A. 1944. The diffraction of X-rays by distorted crystal aggregates-I. *Proceedings of the Physical Society* 56:174–181.
- Thompson P., Cox D., and Hastings J. 1987. Rietveld refinement of Debye-Scherrer synchrotron X-ray data from Al<sub>2</sub>O<sub>3</sub>. *Journal of Applied Crystallography* 20:79–83.
- Tielens A. 2005. *The physics and chemistry of the interstellar medium*. Cambridge: Cambridge University Press.
- Trigo-Rodríguez J. M., Dominguez G., Burchell M. J., Horz F., and Llorca J. 2008. Bulbous tracks arising from hypervelocity capture in aerogel. *Meteoritics & Planetary Science* 43: 75–86, doi:10.1111/j.1945-5100.2008.tb00610.x.
- Tsou P. 2003. Wild 2 and interstellar sample collection and Earth return. *Journal of Geophysical Research* 108:8113, doi:10.1029/2003JE002109.
- Webb S. 2007. *Area Diffraction Machine V2 beta R232*. <https://github.com/joshualande/AreaDiffractionMachine>.
- Welsh B. Y. and Lallement R. 2012. Interstellar gas in the local chimneys. *Publications of the Astronomical Society of the Pacific* 124:566–578, doi:10.1086/666503.
- Westphal A. J., Allen C., Anderson D., Ansari A., Bajt S., Bastien R. K., Bassim N., Bechtel H. A., Borg J., Brenker F. E., Bridges J., Brownlee D. E., Burchell M., Burghammer M., Butterworth A. L., Changela H., Cloetens P., Davis A. M., Doll R., Floss C., Flynn G., Fougeray P., Frank D. R., Gainsforth Z., Grün E., Heck P. R., Hillier J. K., Hoppe P., Hudson B., Huss G., Huth J., Hvide B., Kearsley A., King A. J., Lai B., Leitner J., Lemelle L., Leroux H., Leonard A., Lettieri R., Marchant W., Nittler L. R., Ogliore R., Ong W. J., Postberg F., Price M. C., Sandford S. A., Tresseras J.-A. S., Schmitz S., Schoonjans T., Silversmit G., Simionovici A. S., Solé V. A., Srama R., Stephan T., Sterken V. J., Stodolna J., Stroud R. M., Sutton S., Trieloff M., Tsou P., Tsuchiyama A., Tyliczszak T., Vekemans B., Vincze L., Von Korff J., Wordsworth N., Zevin D., Zolensky M. E., and >30,000 Stardust@home dusters. 2014a. Stardust Interstellar Preliminary Examination II: Optical observations and backgrounds. *Meteoritics & Planetary Science*, doi: 10.1111/maps.12168.
- Westphal A. J., Snead C., Butterworth A. L., Graham G. A., Bradley J. P., Bajt S., Grant P. G., Bench G., Brennan S., and Pianetta P. 2004. Aerogel keystones: Extraction of complete hypervelocity impact events from aerogel collectors. *Meteoritics & Planetary Science* 39: 1375–1386.
- Westphal A. J., Allen C., Anderson D., Ansari A., Bajt S., Bastien R. K., Bassim N., Bechtel H. A., Borg J., Brenker F. E., Bridges J., Brownlee D. E., Burchell M., Burghammer M., Butterworth A. L., Changela H., Cloetens P., Davis A. M., Doll R., Floss C., Flynn G., Fougeray P., Frank D. R., Gainsforth Z., Grün E., Heck P. R., Hillier J. K., Hoppe P., Hudson B., Huss G., Huth J., Hvide B., Kearsley A., King A. J., Lai B., Leitner J., Lemelle L., Leroux H., Leonard A., Lettieri R., Marchant W., Nittler L. R., Ogliore R., Ong W. J., Postberg F., Price M. C., Sandford S. A., Tresseras J.-A. S., Schmitz S., Schoonjans T., Silversmit G., Simionovici A. S., Solé V. A., Srama R., Stephan T., Sterken V. J., Stodolna J., Stroud R. M., Sutton S., Trieloff M., Tsou P., Tsuchiyama A., Tyliczszak T., Vekemans B., Vincze L., Von Korff J., Wordsworth N., Zevin D., Zolensky M. E., and >30,000 Stardust@home dusters. 2014b. Stardust Interstellar Preliminary Examination I: Identification of tracks in aerogel. *Meteoritics & Planetary Science*, doi:10.1111/maps.12168.
- Williamson G. and Hall W. 1953. X-ray line broadening from filed aluminium and wolfram. *Acta Metallurgica* 1:22–31.
- Wojdyr M. 2010. Fityk: a general-purpose peak fitting program. *Journal of Applied Crystallography* 43:1126–1128, doi:10.1107/S0021889810030499.
- Yoder N. C. 2011. PeakFinder. <http://www.mathworks.com/matlabcentral/fileexchange/25500>.
-